MASTER OF SCIENCE THESIS

High Order Adaptively Integrated Cohesive Elements

Development, implementation and testing on composite delamination.

Raffaele Russo

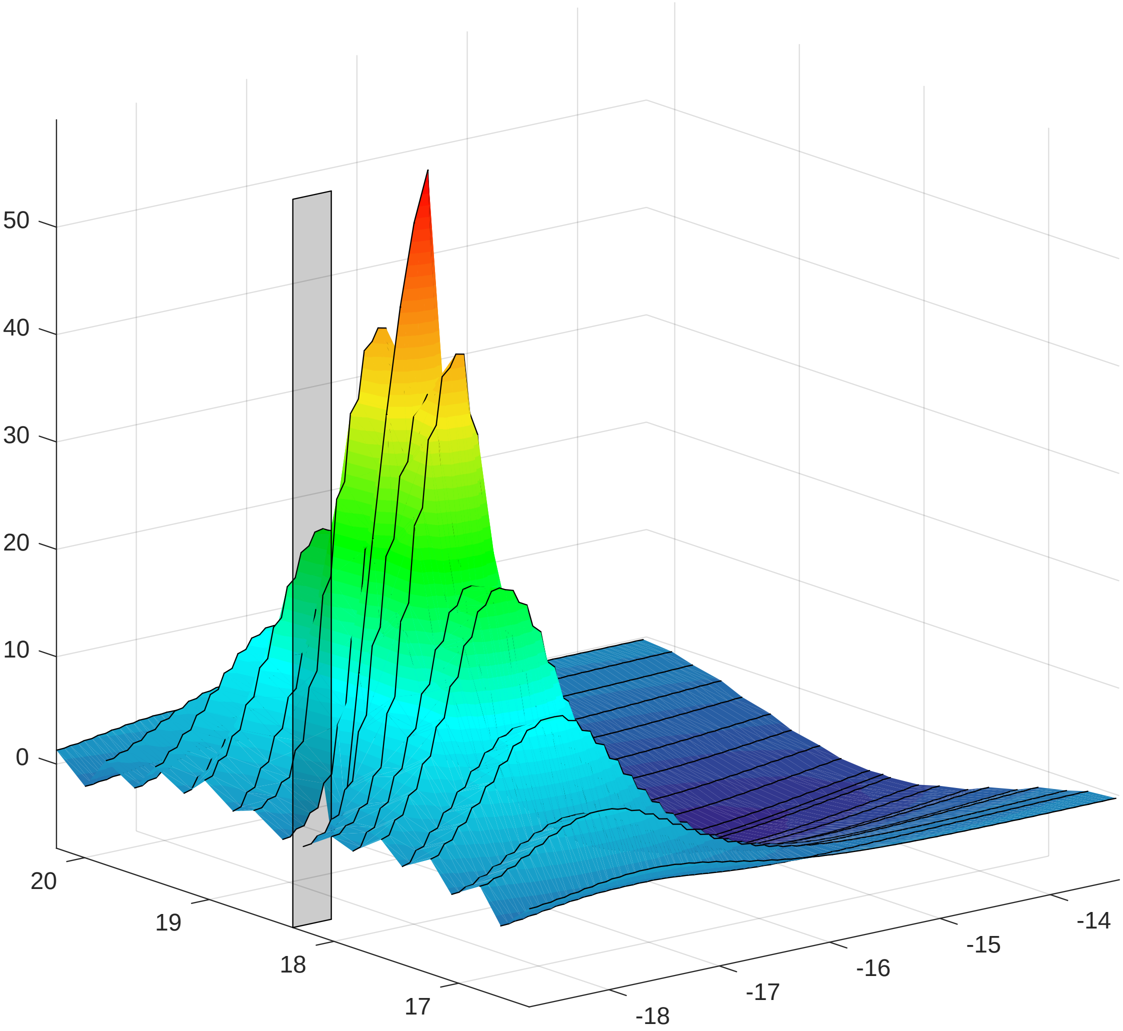

Faculty of Aerospace Engineering · Delft University of Technology

High Order Adaptively Integrated Cohesive Elements

Development, implementation and testing on composite delamination.

MASTER OF SCIENCE THESIS

For obtaining the degree of Master of Science in Aerospace Engineering
at Delft University of Technology

Raffaele Russo

Graduation date

Faculty of Aerospace Engineering · Delft University of Technology

Delft University of Technology
Faculty of Aerospace Engineering
Department of Aerospace Structures and Materials

GRADUATION COMMITTEE

Dated: Graduation date

Chair holder:
Dr. Sergio Turteltaub

Committee members:
Dr. Boyang Chen

Dr. Dimitrios Zarouchas

Abstract

Composite delamination represents one of the most critical failure mechanisms occurring in composite structures. In case complex structures are being designed, numerical methods need to be employed. One of the methods to numerically simulate delamination in a Finite Element environment is through the employment of the Cohesive Elements, which embed the theory constituting the Cohesive Zone Model. Nonetheless, the computational time required to assess delamination simulations by implementing the Cohesive Elements is restrictive, because the presence of a strong stress gradient at the crack tip imposes the adoption of a small-size mesh at the same location. In this contest, a sensible improvement is deemed to be necessary, such as to promote these methodologies from an instrument used in academia to an effective solution. A novel type of Cohesive Element is here proposed, aiming to loosen the compelling requirement on the mesh size and, by extension, to reduce the computational time required to achieve numerical simulation of composite delamination. The High Oder CE has been validated through comparison with benchmark solutions of delamination processes occurring in Mode I, Mode II and Mixed Mode opening.

Table of Contents

List of Figures

List of Tables

Preface

According to Wikipedia, a preface (pronounced "*preffus*") is an introduction to a book written by the author of the book. In this preface I can discuss the interesting story of how this thesis came into being.

This is document is a part of my Master of Science graduation thesis. The idea of doing my thesis on this subject came after a discussion with my good friends Tweedledum and Tweedledee…

Acknowledgments

I would like to thank my supervisor Dr. Boyang Chen for his assistance during the writing of this thesis…

By the way, it might make sense to combine the Preface and the Acknowledgements. This is just a matter of taste, of course.

Delft, University of Technology	Raffaele Russo
Graduation date	

“If we knew what it was we were doing, it would not be called research,
would it?”

— *Albert Einstein*

Chapter 1

Introduction

The demand for low weight/high performance materials from the aerospace industry has been successfully fulfilled by composite materials in the last decades. Composite materials such as glass fibers reinforced plastic (GFRP) or carbon fibers reinforced plastic (CFRP) are asserting themselves as an actual replacement of metals, which, since the advent of the first aircraft, have been widely used to manufacture aircraft structures. Aluminum, being characterized by a high strength-to-weight ratio, represents the natural competitor of composites, and it is therefore the most appropriate element to choose if a trade-off analysis had to be made between metal or composite design.

The main difference between the two materials directly derive from their composition. On one hand, aluminum is made of a homogeneous metal alloy, and it is therefore defined as isotropic material (it provides the same reaction force when loaded from different directions). It has been largely employed because its behaviors are well predictable, as well as its failure modes. On the other hand, composites, due to the fact that they are made of two constituents (fibers and matrix), are anisotropic (they react with different forces, if loaded in different directions) and the know-how related to structural design using composite materials is relatively young with respect to the one related to its metal counterpart.

Nevertheless, composites structures are being employed in aeronautical structures, because they provide an even lighter solution than aluminum. However, the eventual lack of reliable predictions of some of their failure modes is compensated by the employment of knockdown factors during design phase. In structural analysis, the knockdown factors are coefficients used to overcome unforeseen deviations from the conditions which have been hypothesized during the design. The elements which could assume different values than the ones used for design are: the material properties, the expected load and the environmental conditions. In addition to these, further knockdowns might be applied to cover unpredictable failure modes. In particular, one of the most critical and, at the same time, most challenging-to-predict failure, which does not occur in metals, is *delamination*.

Delamination

Delamination is a typical failure phenomenon of composite structures, whose roots lie in the double-constituent nature of the material: fibers and matrix. Diverse techniques are used to manufacture composites, however, the common feature for all of them is that during manufacturing, a resin-rich ply is inevitably created between adjacent fiber layers. The material in this ply is locally characterized by weaker mechanical properties then the one in the fiber-rich zone and therefore more likely to fail. Once it does, delamination occurs: the laminae disbond from each others and the whole structure experiences a big drop of the load-carrying capability.

The failure of the inter-plies matrix will cause the impossibility of the structure to absorb out-of-plane shear, mainly associated to out-of-plane bending, the most severe load case for a composite panel. This phenomenon may occur when the structure is impacted with another object (dynamic load), or when the strength of the inter-plies material is exceeded in a static load application. In the latter case, if the geometry of the structure is such that the stress is non-uniformly distributed, then local stress concentrations arise in the critical zones of the structure, which may locally lead to premature delamination, and subsequently structure failure.

The discipline that studies delamination and, in general, the physics of a fractured continuum is called *fracture mechanics*, a branch of continuum mechanics. The standardized conditions in fracture mechanics in which delamination may occur are called *opening modes*, due to the fact that two adjacent laminae experience a different displacement, or opening (Figure 1.1). Every opening mode is characterized by its own set of three physical properties describing the phenomenon, that are: the stiffness, and therefore the force, that will counteract to the opening, the maximum stress achievable in the opening layer and the final stress before complete failure of the matrix. The different opening modes are labeled as Mode I (normal opening), Mode II and Mode II (shear opening).

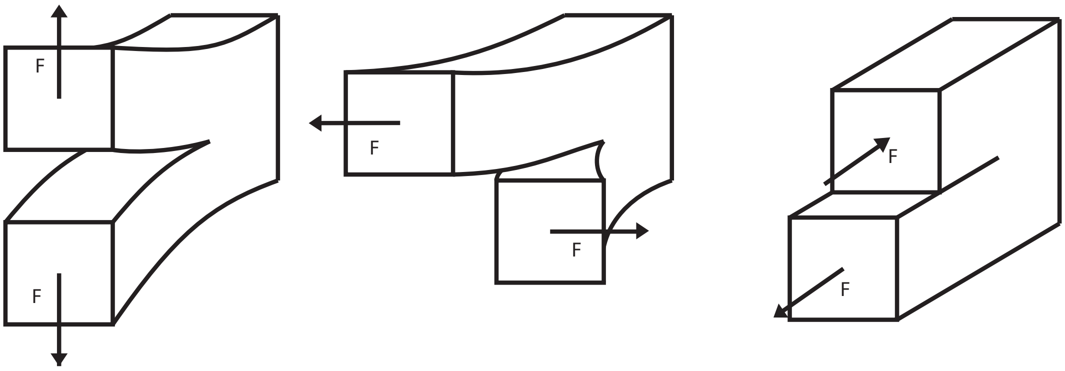

Figure 1.1: From the left to the right, opening mode I, II and III.

Delaminations are particularly dangerous because they are not visible damages, and by the time that a visual inspection could detected them, the reduction of the load-carrying capability of the structure has already passed the threshold of a safe-by-design value. Therefore engineers apply severe knockdowns factors to prevent that. The consequences of this choice lead to a sensible over-design of the structure, negatively affecting its total weight, and therefore reducing the margin of improvements (weight-wise) achievable adopting a design in composite material compared to an aluminum one.

During the design stage, however, examinations can be conducted so to predict whether or not, within the load spectrum foreseen for that structure, delamination will occur. Given that in most of the cases engineers are called to design complex-geometry structures which are dissimilar to the perfect geometries hypothesized in analytical models, numerical procedures aiming to predict delamination, i.e. *Finite Element Analysis* (FEA) assume big relevance.

It is noteworthy to mention that, however, these numerical analysis require not-negligible amount of time to be processed. Both because of the highly non-linear phenomena that are simulated and because of the heavy mesh refinement necessary to capture the same phenomena. In this contest, a sensible improvement is deemed to be necessary, such as to promote the numerical methodologies employed in predicting composite delamination from an instrument used in academia to actual practice, achievable in reasonable amount of time, on which engineers can rely during the design stage.

Research Objective & Methodology

The research pursued as MSc Thesis can be thought to as the attempt in delivering a reliable tools capable of assessing delamination within timespan much less then the one that the actual technology requires. While the research objective can be exemplified as :

> *Enhancement of the limits of applicability of the Cohesive Zone Modelling to numerical fracture mechanic by delivering a novel solution, such that numerical analysis of composite delamination would require less time to be assessed.*

three research questions have been identified:

- Which is the variable/set of variables that has the major influence in limiting the Cohesive Zone Modelling applicability?
- What are the features that still have room for improvement in the Cohesive Zone Modelling approach, and which ones cannot be modified?
- What is the minimum allowable mesh size (maximum computational time), defined by industry best practice, that would set the ultimate goal to be achieved?

The research has been broke down into several stages, such as to create a schematic and organized approach, with the achievement of the final result depending upon the successful completion of each of the following steps:

1. Acquiring a solid knowledge regarding Cohesive Zone Modelling and Cohesive Elements, focusing on the theory behind the models;
2. Select a sample from literature that serves as benchmark;
3. Reproduce the simulations of the benchmark and measure the computational time;

4. Produce a feasible solution to the problem;
5. Acquire knowledge and skills relative to the selected programming language;
6. Implement the solution in the solver;
7. Test the practicability and usefulness of the adopted solution;
8. Measure and evaluate the improvement.

Report structure

In the document that follows the author will give further details regarding the current methods used to predict delamination, the pitfall of these methods and then the results of the research conducted in the last year will be presented, as well as the validation and verification of the model developed. In chapter 2 the numerical technologies used to assess delamination prediction will be examined. The limitations of each will be discussed and a trade-off will be made which will shred light on the reasons behind focusing on one of them only. Subsequently, a well-rounded analysis about the main limitation affecting the employment of the latter technique to assess composite delamination will be provided in chapter 3, followed by a small detour among the solutions previously adopted by other authors attempting to overcome the limitation, from which the author took inspiration. The models proposed by the writer will be exhaustively described in chapter 4, and in chapter 5 the verification and the validation of the models will be provided. Finally, the last part will include the conclusions and recommendation for future development.

Chapter 2

Numerical methodologies to simulate Delamination

The classical theories describing the behavior of continuum are valid under the hypothesis that no interpenetration of material nor crack is present within the body under examination, that is, the control volume. This condition is ensured by the fact the function describing the position of the material in the space is bijective, that is, every position of the control volume is occupied by one and only one particle of material. Once this hypothesis does not hold anymore, the field equations must be reviewed and the numerical methodologies must be adapted as well.

Two classes of numerical methods can be identified, the first one adopting solutions based on energy considerations in a *Linear Elastic Fracture Mechanics* (LEFM) environment, and the other one attempting to model the interaction between the two substrates through damage localization at the delaminated crack tip, that is, *Cohesive Zone Modeling* (CZM). The most used and representative techniques from both the categories are respectively the *Virtual Crack Closure Techniques* (VCCT) and the *Cohesive Elements* (CE).

2.1 Linear Elastic Fracture Mechanic

As suggested by its name, the set of equations used to describe the fracture in a continuum, according to this method, holds under the hypothesis of linear behavior of the material, that it, it does not plastically (irreversibly) deform and its mechanical properties do not suffer any damage.

The first step toward the LEFM theory was done by Alan Arnold Griffith in the attempt to explain the failure in brittle materials (Griffith, 1921).Subsequently, George Rankine Irwin modified the theory such that the material plasticity was taken into account in the energy balance, therefore extending the theory also to ductile materials such as metals (Irwin, 1957).

Furthermore, Irwin noticed that the energy required for the crack to grow if the plastic zone around the crack was smaller that the crack extension, was not influenced by the presence of the plastic zone itself. Therefore, this amount of energy could have been computed as the variation of strain energy per unit of crack length propagated in a material assumed to behave still as linear elastic.

Since the Irwin's observation, several techniques have been developed to compute the amount of work required for the crack to be closed back, they differentiate from each other in the way this quantity is computed. The method that follows dates back to 1977, and since then, it has been widely used to numerically simulate the fracture process.

2.1.1 Virtual Crack Closure Technique

The VCCT is based on the LEFM theory, it was first proposed as a method to compute the energy strain energy release rate by Rybicky and Kanninen (Rybicki and Kanninen, 1977). This approach is based on a simple energy consideration made by Irwin: the energy released while extending the crack of a finite length, is equal to the energy required to close the crack by the same length (Figure 2.1).

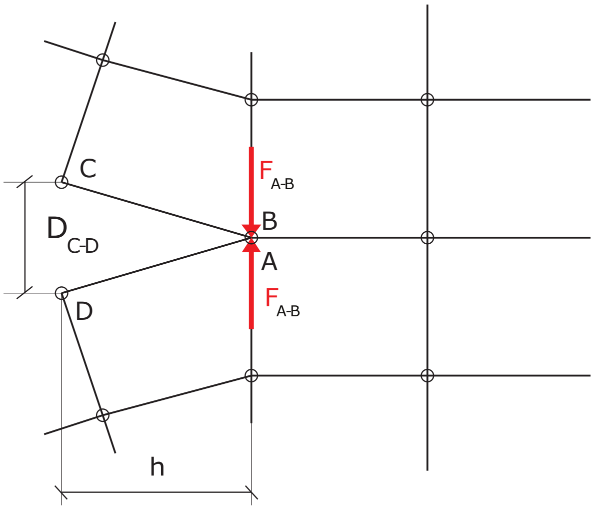

Figure 2.1: VCCT scheme.

Referring to Figure 2.1, Rybicky and Kanninen proposed to numerically evaluate the energy required to close the crack as follows:

$$G = \frac{F_{AB}\Delta_{CD}}{2hw} \tag{2.1}$$

In fracture mechanics the letter G refers to the strain energy release rate, whose units are in $\frac{J}{m^2}$, the distribution of energy within a unit area. F_{AB} is the closure force at the nodes A and B, Δ_{CD} is the normal opening between the nodes C and D, h is the length of the mesh element and w is the width of the element (out-of-plane dimension).

According to LEFM, the crack starts propagating when the following condition is met:

$$G = G_c \tag{2.2}$$

The critical level of energy, indicated as G_c in Equation 2.1 is known as *fracture toughness*. It is a material property, and it characterizes whether a material behaves as brittle or ductile during a fracture process. The highest the fracture toughness, the more the energy that the material requires for the crack to propagate. High level of strain energy are achieved in materials which undergo plastic deformation and therefore exhibit a ductile behavior. On the contrary, materials that are characterized by small values of fracture toughness are the one which do not experience plastic deformation and therefore behave as brittle.

The strain energy release rate, as well as the fracture toughness, characterize the behavior of the material when fracture occurs. However, in anisotropic or orthotropic materials, this property might assume different values depending on the direction in which the crack is propagating, that is, the fracture process might assume different configurations, i.e. fracture modes. It follows that a specific value of the critical strain energy release rate is associated with each and every mode, therefore leading to a triad of values necessary to identify the fractural behavior of a composite structures. Every value of the strain energy release rate is directly compared with its critical one, and no mixed-influence between modes is modelled using VCCT.

From the FEA perspective, the implementation of this technique requires the user to know beforehand the path that the crack will follow, because he has to select the nodes eligible for the opening process, such that for each of them the quantity in Equation 2.2 could be computed and compared with its respective critical value. It should be clear that no material softening can be simulated using the VCCT. The joint between the nodes in contact holds until the condition is met. Once the energy reaches the critical value, the rigid connection between the nodes is drastically removed, causing the structure to experience a sudden drop of stiffness.

2.2 Cohesive Zone Modeling

The CZM is a modeling technique proposed in the early 60’ by Dugdale (Dudgale, 1960) and Barenblatt (Barenblatt, 1962), which was initially employed to describe the material non-linearity near notches. The main difference from the LEFM lies in the way the process of fracture is approached. The CZM aims to explicitly model the continuous and irreversible damage process characterizing the material in front of the crack tip, therefore considering, and actually focusing only on the process characterizing the area commonly referred to as *Cohesive Zone* (CZ), which the LEFM clearly and intentionally neglects.

Even though the CZM has been originally developed to cope with plasticity in ductile materials as metals, it has been widely employed to simulate fractures in brittle materials, e.g. composites. In fact, in a CZM fashion, the softening phase that the resin-rich layer in a composite structure undergoes to, can be modeled through the employment of interface elements, which provide a traction between the separating surfaces. The softening of the cohesion is achieved through the employment of a specific law, i.e. *cohesive law*, characterizing the relationship between the opening and the traction provided by the material within the CZ.

2.2.1 Cohesive Law

Several cohesive models have been proposed in literature to characterize the traction-separation coupling, having different shapes such as linear, bilinear, polynomial, linear-exponential and so on (Tvergaard and Hutchinson, 1992; Cui and Wisnom, 1993; Needleman, 1987) (Figure 2.2). However, due to its simple description, the bilinear model (Figure 2.2b) has been widely adopted in the literature. Regardless of the shape of the cohesive law, the most particular feature of this law is that it couples the traction or the stress with the opening, while, in the classical continuum mechanics, the constitutive laws couple the stress with the strain.

The influence of the shape of the cohesive law on the global structural response has been investigated by several authors (Yang and Cox, 2005; Shet and Chandra, 2004) and they concluded that its shape exhibit a small and negligible influence as long as the area under the curve is equal to G_c, and the fracture process zone is small compared to the structural dimension.

In the bilinear model, the cohesive behavior is initially characterized by a linear-elastic phase, and, after damage initiation, the softening process takes place, during which the damage propagation is simulated. The damage progression within the CZ is therefore simulated through a linear reduction of the stiffness of the material. While the first part has only been successively added to provide smoothness to the numerical solution before damage initiation, more emphasis is given to the second phase, since it is the one which is actually employed to simulate the damage progression.

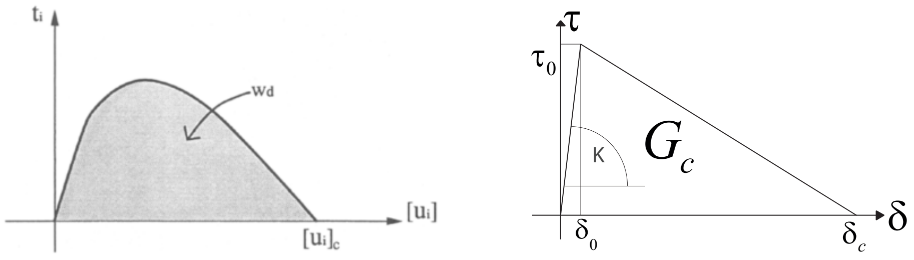

(a) Elasto-plastic cohesive law. **(b)** Bilinear cohesive law.

Figure 2.2: First draft of CE constitutional law (a)(Corigliano, 1993), and bilinear constitutional law (b).

In the same way the implementation of the VCCT requires three values of the fracture toughness, one for each opening mode, so there are three distinct cohesive laws characterizing the deterioration of the stiffness of the material, one for each opening mode. To uniquely characterize the behavior of the material within the CZ, that is, the cohesive law, three sets, of three properties each, must be defined:

- G_c;
- τ_0.
- K;

G_c is the fracture toughness, τ_0 is the material strength (the maximum stress the material can witstand), finally, K is the initial stiffness of the material. For every opening direction, the respective cohesive law must be delineated by mean of a triad of these parameters. While the fracture toughness and the material strength are properties which can be extrapolated from tests, the penalty stiffness is something different, which will be further analyzed in the context of delamination.

2.2.2 Cohesive Elements

The employment of the CZM technique in a FEA environment could be done through several ways, but the solution which presents less disadvantages and more adaptability is to adopt a special purpose element called *Cohesive Elements* (CE), whose characterization directly follows the CZM theory. The analytical model of the CEs went through a refinement process in which several authors gave their contribution (Mi et al., 1998; Alfano and Crisfield, 2001; Camanho and Davila, 2002; Turon et al., 2006, 2010).

They have modeled the CE mechanical behavior by employing the bilinear constitutional law to couple openings and traction. In Figures 2.3 and 2.4 the general 2D and 3D cohesive elements are depicted. Within the scope of this research, the CEs are used to simulate delamination, therefore their initial configuration would be different then than the one pictured in Figures 2.3 and 2.4. They would, in fact, have zero initial thickness.

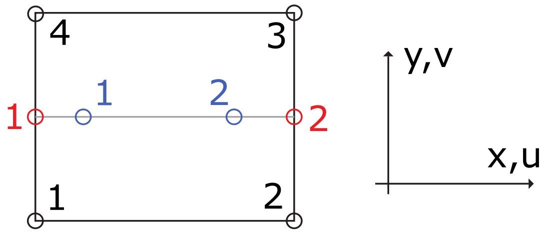

Figure 2.3: 2D CE.

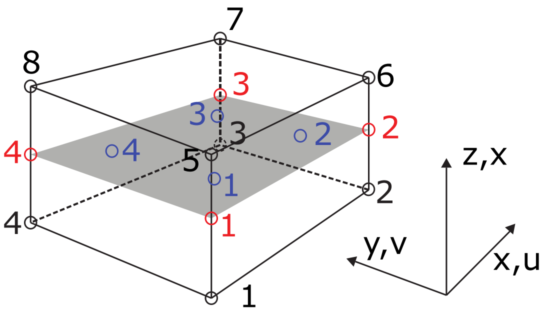

Figure 2.4: 3D CE.

In the Figures 2.3 and 2.4 several constituents may be observed. The black circles represent the nodes, same color has been used to indicate their numbering. The other circles represent the locations at which the parameters of the CEs (separation and respective traction) are evaluated in a FEA environment, i.e. *integration points*. The positions of the red circles are determined by a *Newton-Cotes* type of integration scheme, while for the blue ones, a *Gaussian* type of integration scheme has been adopted.

The CEs are used as framework to implement the cohesive behavior. The nodal separations of the CEs are computed such as to be representative of the three opening modes identified in fracture mechanics (Figure 1.1), and, referring to Figure 2.4, they are expressed as follows:

$$\delta_n = w_{i+4} - w_i, \qquad i = 1,2,3,4 \tag{2.3}$$

$$\delta_s = v_{i+4} - v_i, \qquad i = 1,2,3,4 \tag{2.4}$$

$$\delta_t = u_{i+4} - u_i, \qquad i = 1,2,3,4 \tag{2.5}$$

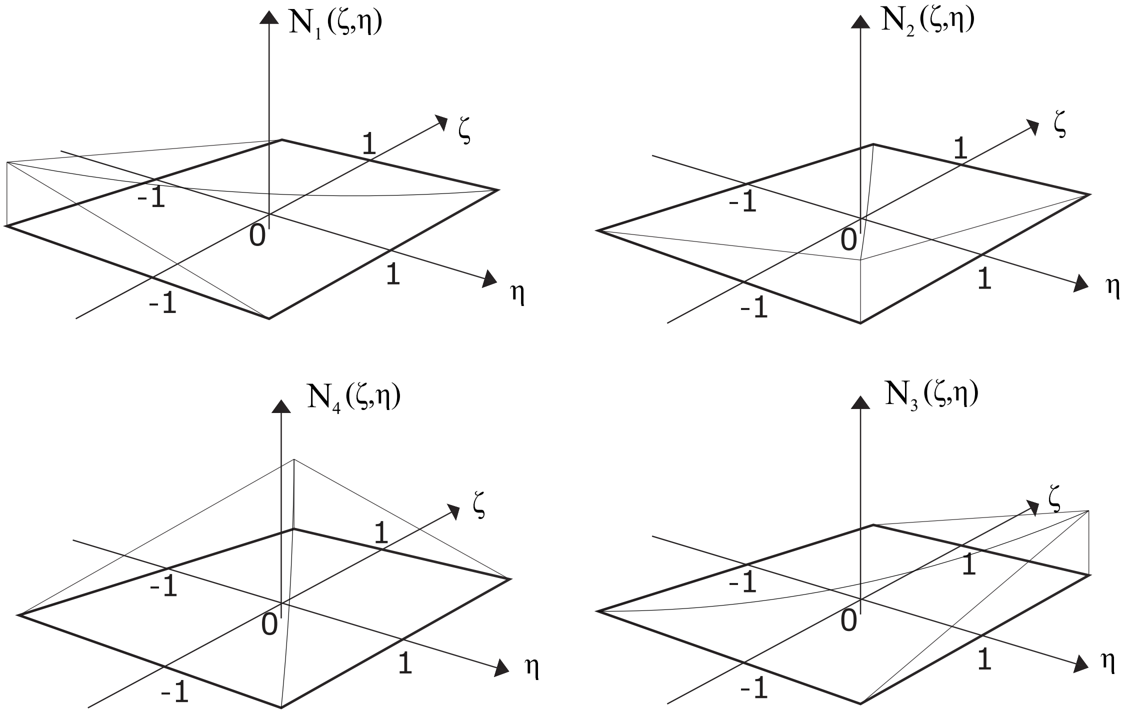

Figure 2.5: Shape functions used in a 3D CE.

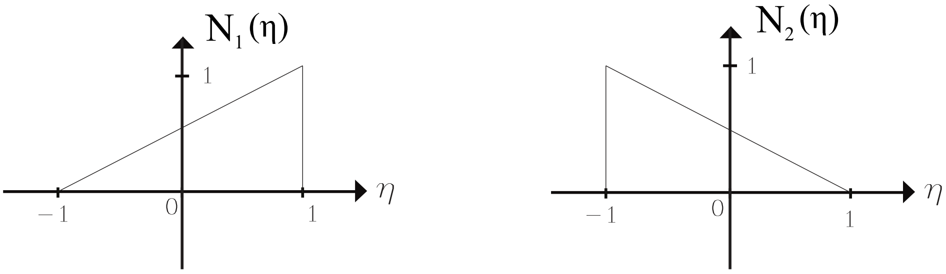

Figure 2.6: Shape functions used in a 2D CE.

The w_i, v_i and u_i are the nodal coordinates of the i^{th} node along the axis z, y and u respectively. The domain of definition of the CE is the gray line in Figure 2.3 and the gray plane in Figure 2.4, representing the mid-line or mid-plane of the element. In the local frame of reference, i.e. $\{\zeta$ - $\eta\}$ in 3D or η in 2D, the domain of definition spans between [-1;1]; the openings and the respective tractions are defined within this domain. In the typical FEA fashion, the displacement fields of the CE is evaluated as interpolation of nodal values. For this element, linear functions are employed, whose representation can be observed in Figures 2.6 and 2.5.

Moreover, the definition of the mid-plane or mid-line of the element is fundamental to identify the correlation between the openings of the CEs and the openings related to the fracture modes. For instance, the unit vector orthogonal to the mid-plane/mid-line indicates the direction along which normal opening is developing. The latter unit vector, together with two other unit vectors, being orthogonal each other and mutually orthogonal to the normal one, define the local frame of reference of the CE. In this reference system, the opening fields within the CE domain are defined as:

$$\delta_n(\zeta,\eta) = \begin{bmatrix} N_1(\zeta,\eta) & N_2(\zeta,\eta) & N_3(\zeta,\eta) & N_4(\zeta,\eta) \end{bmatrix} \cdot \begin{bmatrix} \delta_{n_1} \\ \delta_{n_2} \\ \delta_{n_3} \\ \delta_{n_4} \end{bmatrix}$$

$$\delta_s(\zeta,\eta) = \begin{bmatrix} N_1(\zeta,\eta) & N_2(\zeta,\eta) & N_3(\zeta,\eta) & N_4(\zeta,\eta) \end{bmatrix} \cdot \begin{bmatrix} \delta_{s_1} \\ \delta_{s_2} \\ \delta_{s_3} \\ \delta_{s_4} \end{bmatrix} \tag{2.6}$$

$$\delta_t(\zeta,\eta) = \begin{bmatrix} N_1(\zeta,\eta) & N_2(\zeta,\eta) & N_3(\zeta,\eta) & N_4(\zeta,\eta) \end{bmatrix} \cdot \begin{bmatrix} \delta_{t_1} \\ \delta_{t_2} \\ \delta_{t_3} \\ \delta_{t_4} \end{bmatrix}$$

Where in δ_{i_j}, the i refers to one of the three openings, and j indicates that the opening is evaluated at the node j. As previously anticipated, the CEs embed the Cohesive Law to characterize the material response. The openings are coupled to the tractions that the CEs provide in the following way:

$$\begin{pmatrix} \tau_n \\ \tau_s \\ \tau_t \end{pmatrix} = D \begin{bmatrix} K_n & 0 & 0 \\ 0 & K_s & 0 \\ 0 & 0 & K_t \end{bmatrix} \begin{pmatrix} \delta_n \\ \delta_s \\ \delta_t \end{pmatrix} \tag{2.7}$$

Where D is the variable accounting for the damage of the CE, this variable is dependent on the status of the opening and will be thoroughly investigated later. From Equation 2.7 it can be inferred that the CEs show no coupling between the opening modes. The openings are computed in global directions and then evaluated in the local reference system. The values of the local openings are then plugged into the cohesive law, subsequently, the traction provided by the CE is evaluated.

The initial element stiffness K is a numerical artifact introduced to improve the smoothness of the solution. Therefore its value is not related to any material mechanical property. However, in case the CE are used to model delamination, Turon et al. provided a handful equation to choose the value of K (Turon et al., 2007). Driven by physical considerations, the following relation had been proposed:

$$K = \alpha \frac{E_3}{t} \tag{2.8}$$

Where E_3 is the laminate Young modulus along the out-of-plane direction, t is the laminate thickness, and α is a constant used to properly tune the value of K, such that a one-variable-only dependence can be implemented. On one hand, too large values of α lead to oscillations in the simulations, on the other hand values too small lead to material too soft, and the stress does not localize in the CEs. In their research, Turon et al. convened that 50 would be an appropriate value.

A further simplification of the CEs is the one proposed by Camanho et al., suggesting to treat the two openings in the shear direction (corresponding to mode II and mode III opening) on an equal footing, and therefore to use the same properties to build their constitutive laws:

$$\begin{gathered} \delta_{sh} = \sqrt{(\delta_s)^2 + (\delta_t)^2} \qquad \tau_{0_s} = \tau_{0_t} = \tau_{0_{sh}} \qquad K_s = K_t = K_{sh} \\ G_{c_t} = G_{c_s} = G_{c_{II}} = G_{c_{III}} = G_{c_{sh}} \end{gathered} \tag{2.9}$$

The employment of the CZM to simulate delamination employing CEs narrows down to the modelling of the damage afflicting the material within the CZ. As previously anticipated, the degradation is assessed though the employment of the Cohesive Law as constituent law of the material. The stiffness of the CE linearly decreases toward its complete annihilation. Referring to Figure 2.2b, the damage variable, d, ranging from 0 (intact material) to 1 (completely damaged), is a function of the opening status of the CE:

$$d = \frac{\delta_f(\delta - \delta_0)}{\delta(\delta_f - \delta_0)}, \qquad \delta \in [\delta_0; \delta_f] \tag{2.10}$$

The onset of delamination is meant to be predicted once the traction that the CE experiences is equal to the material strength (τ_0). The softening of the CE takes place and, with ever increasing openings, the stiffness of the material deteriorates and eventually goes to zero. The damage variable D is equal to $(1 - d)$, such that it linearly varies from one to zero. For opening conditions that lie outside the domain of definition of d, the variable D is directly implemented as 1 or 0 depending on the opening status. The values of the critical opening, δ_f, is computed as follows:

$$\delta_f = \frac{2G_c}{\tau_0} \tag{2.11}$$

In case the CE is subject to pure mode I/ mode II opening, then the definition of the damage variable is trivial. It is not the case when the CE is experiencing a Mixed Mode Loading.

Mixed mode loading

Once all the parameters of the constitutive laws governing pure mode I and pure mode II/III loading have been established, it is possible to define the mixed-mode loading condition. In the extensive work done by Turon et al. (Turon et al., 2006), they proposed a thermodynamically consistent damage model, which accounts for changes of the mixed mode loading condition. The procedure consists in first identify in which degree the opening that the CE is experiencing is mixed between pure mode I and II through the definition of β, the *mode mixity ratio*, and then to define the cohesive law based onto the actual mode mixity ratio:

$$\delta_m^2 = \langle \delta_n \rangle^2 + \delta_{sh}^2 \tag{2.12}$$

$$\beta = \frac{\delta_{sh}}{\delta_m} \tag{2.13}$$

$$B = \frac{G_{shear}}{G_T} = \frac{\beta^2}{1 + 2\beta^2 - 2\beta} = \frac{\delta_{sh}^2}{\delta_m^2} \tag{2.14}$$

$$\delta_{0_m}^2 = (\delta_{0_n})^2 + [(\delta_{0_{sh}})^2 - (\delta_{0_n})^2]B^\eta \tag{2.15}$$

$$\delta_{f_m} = \frac{\delta_{0_n}\delta_{f_n} + (\delta_{0_{sh}}\delta_{f_{sh}} - \delta_{0_n}\delta_{f_n})B^\eta}{\delta_{0_m}} \tag{2.16}$$

$$\tau_{0_m} = K\delta_{0_m} \tag{2.17}$$

$$G_{c_m} = G_{c_I} + (G_{c_{II}} - G_{c_{III}})B^\eta \tag{2.18}$$

$$d = \frac{\delta_{f_m}(\delta_m - \delta_{0_m})}{\delta_m(\delta_{f_m} - \delta_{0_m})} \tag{2.19}$$

$$\tau = (1 - d)K\delta \tag{2.20}$$

Where δ_m is the mixed-mode separation of the interface, $\delta_{0_{sh}}$ and δ_{0_n} are the critical openings in pure mode II and I, G_{shear} and G_T are the strain energy release rate in the shear direction and the total energy release rate ratio, δ_{0_m} is the critical mixed-mode separation, τ_{0_m} is the respective critical traction and δ_{f_m} is the final mixed-mode opening. The brackets $\langle\rangle$ indicate the MacAuley operator, which returns the input in case it is positive, and zero otherwise. The mixed-mode fracture toughness, G_{c_m} is defined according to the Benzeggagh and Kenane (B-K) model, which requires the material property η to be evaluated (Benzeggagh and Kenane, 1996).

Successively, another improvement has been done on the model. Turon et al. pointed out that, during loading processes, due to the variation of the critical strain energy release rate caused by a change of the mixity mode ratio, re-healing of the material could have occurred if the material properties of the CE was not properly chosen. In particular, they developed a methodology to choose the values of some mechanical properties of the CE such that the variable damage monotonically grew in time (Turon et al., 2010). Depending on whether the material is brittle or ductile, they proposed either to modify the strength of the material in pure mode II ($\tau_{0_{sh}}$) or adopt a different value for the shear penalty stiffness (K_{sh}) respectively, according to the following:

$$\tau_{0_{sh}} = \tau_{0_n} \sqrt{\frac{G_{c_{II}}}{G_{c_{III}}}} \tag{2.21}$$

$$K_{sh} = K_n \frac{G_{c_I}}{G_{c_I}} \frac{\tau_{0_{sh}}^2}{\tau_{0_n}^2} \tag{2.22}$$

As explained before, when a material behaves as ductile during a fracture process, the CZ is much larger then the one associated to brittle fracture. This leads to a not-anymore-negligible dependency of the results of the simulation on the shape of the cohesive law, consequently, on the penalty stiffness. However, since composites behave as brittle, the suggestion is to adopt Equation 2.21 instead of 2.22, and therefore choose the shear strength of the CE accordingly, to avoid unreal healing of the material.

2.3 Comparison VCCT and CEs

Besides the considerations related to the mesh size, which is the topic of the next chapter, several are the elements on which a confront can be made between these two techniques to numerically simulate fractures.

The main difference between the two methods is that while employing the VCCT the crack path must be known a priori, using CEs could bring the crack to propagate throught the thickness, therefore including the possibility to model multiple delamination propagation or through-the-thickness delamination migration (Chen et al., 2016). This represents the major limitation of VCCT implementation, and the whole gap left by the VCCT is covered by the CEs.

Another difference is related with the nature of the numerical fracture process. The approach based on LEFM constrains two nodes to be coincident until a critical condition is met, after which the two nodes previously attached suddenly detach. This leads to a sudden change of the geometrical configuration of the structures ans a subsequent instantaneous drop of the structural stiffness. On the contrary, the process simulated employing CEs is continuous, and the same holds for the variations in geometry, strain and stress. The sudden drops of stiffness have amplified consequences the more the mesh size increases, therefore, this drawback imposes to use a very small mesh size if smaller scale phenomena must to be captured in the simulation.

A comparison could also be made regarding the type of fractures that can be simulated. The VCCT, based on LEFM principles and considerations, can only be employed to simulate brittle fractures, since the hypothesis of small CZ must hold. The same limitation does not apply to CEs, because the mechanical properties characterizing the response of the CE can be tuned such as to comply with ductile fractures as well.

The ability to simulate the thickness of the adherent between two materials can also be added to the comparison. The VCCT does not comply with non-zero-distance between two substrates, while the CE formulation is compatible with the condition of finite thickness of the adherent.

The last remarkable comparable feature between the two methods is the dependency that the VCCT shows on the numerical discretization of the continuous loading process simulated. The reason is that the configuration of the structure is updated at every increment in which the loading as been decomposed, and only one bond per increment can be deleted. On the contrary, since the CE status is based on the openings that characterize it, the possibility of fully damaging more than one CE per increment is not precluded.

One particular advantage, though, in using the VCCT is that its implementation seems to be more direct and, moreover, it requires less inputs and therefore less tests to be done on the material to extrapolate some mechanical properties such as its strength.

Chapter 3

Problem Definition

The main limitation affecting the modeling of composite delaminations with CEs, lies in the restriction on the mesh size (Moës and Belytschko, 2002; Yang and Cox, 2005; Turon et al., 2007; Harper and Hallett, 2008; Yang et al., 2010; Turon et al., 2010; Harper et al., 2012; Do et al., 2013; Li et al., 2014; Álvarez et al., 2014; Pirondi et al., 2014). Due to the geometric discontinuity, a strong stress gradient is present at the crack tip (Figure 3.1), and if CEs are used to simulate delaminations, their mesh size at this location must be dense enough to catch the stress variation. When simulating crack growth, the crack tip moves along the CEs, therefore extending the mesh-size constraint to all the CEs involved.

Other techniques which are used to simulate delamination are inadequate as well when the mesh size becomes too large. Indeed, if VCCT is used with a too coarse mesh, the drop in the stiffness of the structure would be too severe every time an element opens and the frequency of breaking bonds would be too low to ensure a good simulation. The reproduced structural behavior would be affected by strong discontinuities , even though in the reality it is smooth.

The effect of choosing the wrong element size can be observed in the predicted normal stress distribution at the crack tip in a DCB specimen in Figure 3.2.

The area over which the stress gradient is strong is called *Cohesive Zone Length* (CZL) or *Cohesive Length* (CL). This characteristic length is much smaller than the typical dimensions of a composite structure (the average value is in the order of magnitude of millimeters), and the meshing of the whole structure is affected by the limitation this zone is constrained to. Several authors have given suggestions on the minimum number of elements required within the CZL. Harper and Hallett suggested a number of elements larger or equal than 3 (Harper and Hallett, 2008). Moes and Belytschko proposed 10 elements (Moës and Belytschko, 2002). Camanho and Davila used approximately 3 elements within the CZL (Camanho and Davila, 2002). Yang and Cox suggested to use from 3 to 5 elements (Yang and Cox, 2005). Therefore, in literature significant importance is given to this length and various are the efforts done to correctly estimate it.

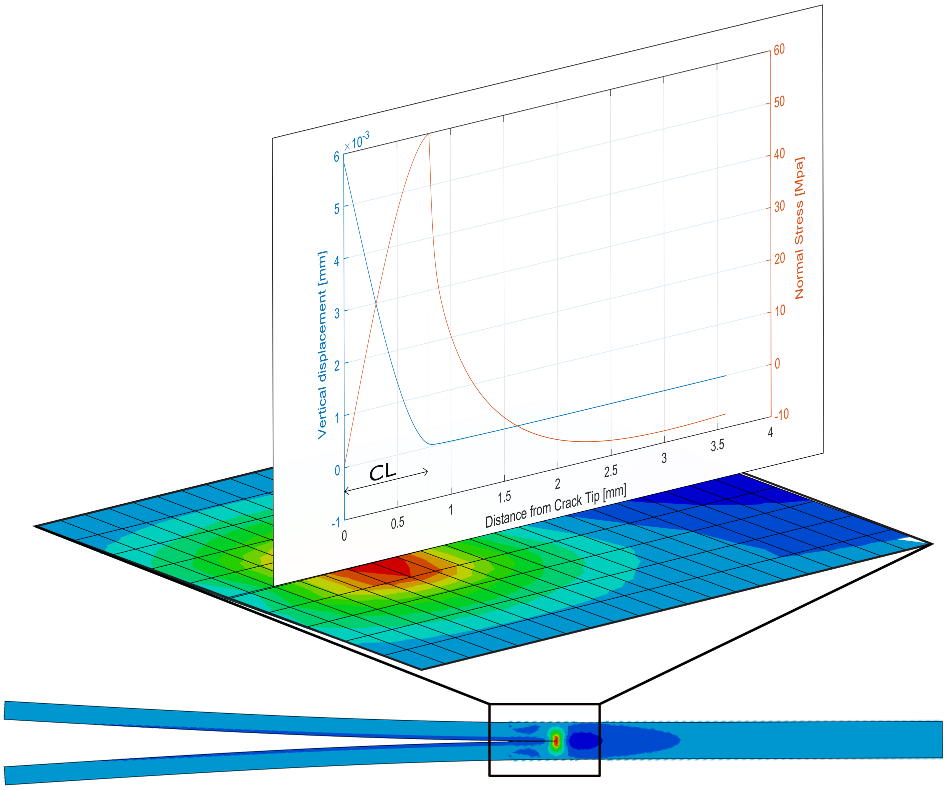

Figure 3.1: Normal Stress distribution in a row of CE used in a DCB test.

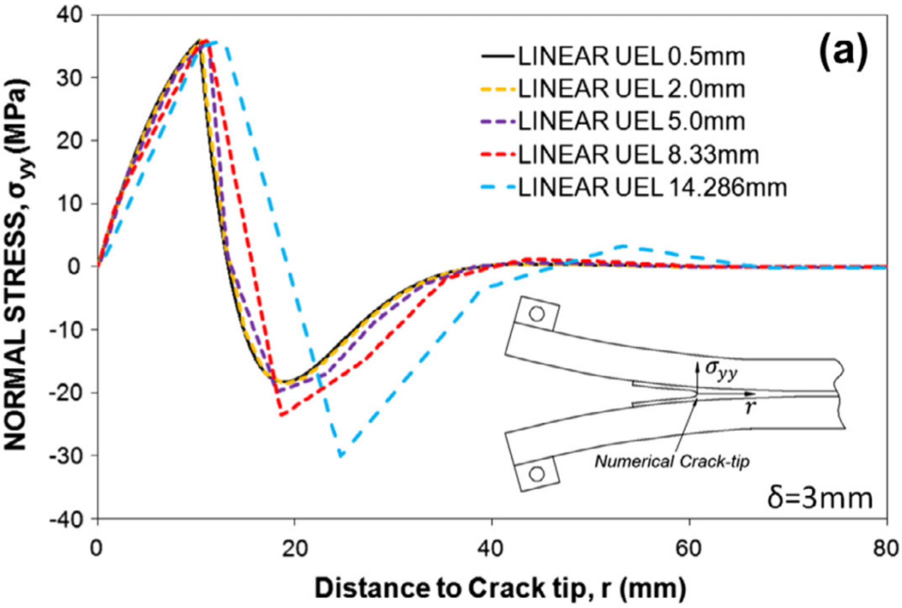

Figure 3.2: Normal stress at the crack tip predicted using different mesh sizes (Álvarez et al., 2014).

M	Authors
$\frac{2}{3\pi}$	Hui et al. (Hui et al., 2003)
$\frac{n+1}{\pi}$	Bazant et al. (Bazant and Planas, 1997)
$\frac{1}{\pi}$	Irwin (Irwin, 1997)
$\frac{\pi}{8}4$	Barenblatt (Barenblatt, 1962), Dugdale (Dudgale, 1960)
$\frac{\pi}{4}$	Cox and Marhall (Cox and Marshall, 1994)
$\frac{9\pi}{32}$	Rice (Rice, 1979), Falk et al. (Falk et al., 2001)

Table 3.1: Values of the variable M from different authors.

3.1 Cohesive Zone Length

In literature, several works can be found regarding a correct estimation of the CL through analytical models. This entity has been correctly evaluated in the condition of infinite body and slender body. In the former case, the CZL depends only on the material properties, in the latter case the CZL shows dependency on geometry of the structure, besides material mechanical properties and loading condition (mixity mode ratio). A fundamental quantity, which can be found throughout the literature related to CZL, has been introduced by Hillerborg et al. (Hillerborg et al., 1976), it is presented in Equation 3.1, and it embodies the dependencies on material properties and loading condition:

$$l^{\infty}_{ch,i} = \frac{E_i G_{c,i}}{(\tau_{0,i})^2}, \qquad i = I, II, m \tag{3.1}$$

$$E_m = E_I(1 - B) + E_{II} \tag{3.2}$$

The subscript i is highlighting the fact that these quantities must be evaluated according to the loading condition (pure I/II or mixed mode), G_c is the fracture toughness and τ_0 is the material strength and E is the Young modulus relative to the respective loading condition. In case mixed-mode opening is experienced, the Young modulus is evaluated through Equation 3.2, where B is the same variable used to identify the loading mode used in Equation 2.14). The apex ∞ indicates that this value has been attained under the hypothesis of infinite plate.

The CZL shows dependency also on the loading condition, and, among the three fracture modes, mode I opening is usually characterized by the smallest CL. Therefore, several authors presented models to predict the CZL in mode I, and they all developed solutions whose form is given in Equation 3.3. Every author used a different value of M (Table 3.1), but it has been concluded that, however, its value only depends on the cohesive law used to characterize the material (Soto et al., 2016).

$$l^{\infty}_{czl,I} = M l^{\infty}_{ch,I} \tag{3.3}$$

Besides the solutions developed under the hypothesis of infinite body, the problem has been approached considering a body as slender as well:

$$l^0_{czl,I} = M^0_I (l^\infty_{ch,I})^{\frac{1}{4}} t^{\frac{3}{4}}; \qquad (3.4) \qquad\qquad l^0_{czl,II} = M^0_{II} \sqrt{l^\infty_{ch,II} t}. \qquad (3.5)$$

Where t is the laminate thinness The Equations 3.4 and 3.5 have been respectively developed by Smith (Smith, 1989) and Massabó and Cox (Massabo and Cox, 1999). They used the values of $\frac{1}{3}$ and 2 for M^0, for mode I and mode II respectively.

However, as showed by Harper and Hallett (Harper and Hallett, 2008) and Turon et al. (Turon et al., 2008) the formulas overestimate the CZL, therefore, other solutions have been developed. Two methods are of particular relevance, but they suffer from the limitation to be semi-empirical.

Turon et al. proposed to find the CZL by weighting the solution of the CZL in an infinite body with the thickness of the specimen and a characteristic thickness. The formula in Equation 3.6 holds for mixed-mode loading as well.

$$l_{czl}(h) = \frac{t}{t + h_0} M l^\infty_{ch,i} \qquad (3.6)$$

Where h_0 is a characteristic length which depends on the mixed-mode loading, structure and material (Turon et al., 2008; Bezant and Planas, 1998) and t is the laminate thickness. The values of M and h_0 have been obtain though a non-linear regression of the numerical data.

Soto et al., instead, proposed another method to calculate the CZL. They considered the CZL to be possibly estimated through a particular weighted average between the infinite body CZL (Equation 3.3) and the slender body CZL (Equations 3.4 and 3.5).

$$l_{czl,i} = \left({l^0_{cz,i}}^{n_i} + {l^\infty_{cz,i}}^{n_i} \right)^{\frac{-1}{n_i}}, \qquad\qquad i = I, II \qquad (3.7)$$

The values of the weights and of the variable n in the Equation have been found through least square fitting with experimental data. However, they provided only the equations to estimate the CZL for pure mode loading conditions.

3.2 Previous solutions

Even though the CZL is still not easily predictable, the topic introduced in the previous section serves as to give an idea to the reader about the extent of the zone in which the excessively refined mesh should be concentrated. As previously assessed, smallest values of the CZL are attained in a mode I opening.

Several authors tried to approach this problem, each one proposing a diverse way to overcome the problem and in this section a brief overview of the solutions already present in literature are presented. Most of the works here reported are dated in the last five years, indicating that the topic is still and open discussion and the limitation on the mesh size using CEs is a contemporary problem, that many researcher groups are trying to overcome.

As final remark, for each proposed method, it will be pointed out the maximum CE length to CZL ratio reachable when implementing the proposed technique, which still ensures an error-free simulation. It is necessary to remember what said in the introduction of the present chapter regarding the suggestions made by diverse authors about the number of CE to be used within the CZL, such as to adopt their suggestions as a benchmark and as the limitation which needs to be slackened.

3.2.1 Integration Schemes & Sub-Domain Integration

The authors Yang et al. (Yang et al., 2010), and later also Do et al. (Do et al., 2013), proposed a solution through the employment of a Gaussian integration schemes coupled with *Sub-Domain Integration* on a 3D CE adopting linear shape functions (Figure 3.3). They developed an extensive method to sub-integrate the CE, by initially detecting the sub-domain in which the stress of the CE exceeds the critical value (τ_0) and subsequently performing the numerical integration of the stress field within each sub-domain, therefore achieving an improved prediction of the global strain energy within the CE. The way they propose to track the crack front is through the technology called *Level Set Description*. Meaning that this method allows the integration points to move within the element, and adapt to the partially broken element.

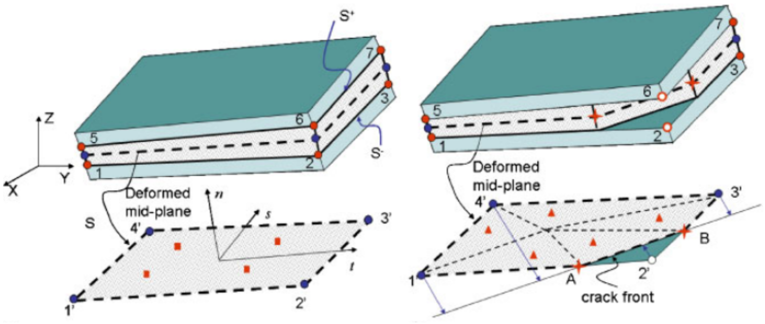

Figure 3.3: Sub Domain Integration procedure (Yang et al., 2010).

In Figure 3.3 the still intact (left) and partially damaged (right) elements are shown. The red squares on the left indicate the standard Gaussian quadrature points, while the red triangles on the right represent the quadrature points of every sub-domain.

However, the results they obtained are still mesh dependent. The authors achieved good predictions of the fracture process in a DCB test employing CEs whose original mesh size is 2.14 times the CZL, while retaining stability and robustness of the solution, which is, however, not smooth. The time gain they achieved was measured by running the same model, using standard CEs and the CEs they developed. For the model used to test the time gain, they adopted a CEs mesh size of 0.28 times the CZL. In this conditions, they attained a CPU time saving of 43.5%.

Level Set Description

In (Yang et al., 2010) the authors employed the *Level Set Description* to track the position of the damage front. This method is used to track the advancement of the crack in a mesh independent way.

An identical domain of the initial meshed structure is created. The damage condition is based on nodal relative openings and their critical values. Since the opening field is obtained as linear interpolation within the domain of the nodal values, so it is the damage condition. Therefore, the crack front can bridge two edges of the element and it is not constrained to pass through the nodes (Figure 3.4).

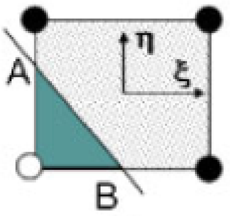

Figure 3.4: Crack front and sub-domain representation (Do et al., 2013).

3.2.2 Strength Reduction

In (Turon et al., 2007) Turon et al. proposed to solve the problem by altering the effective strength of the CE, in particular, reducing it. Referring to Equation 3.1, a lower value of τ_0 leads to larger CZL, therefore larger mesh size of the CE which can be employed. The CE they used are the one developed in (Camanho and Davila, 2002).

The authors, by superimposing that the number of elements in the numerical CZL, i.e. N_{el}, should be equal to the CZL divided by the element size,developed the following equation that computes the strength to be used as input in the CE:

$$\bar{\tau_0} = \sqrt{\frac{9\pi E G_c}{32 N_{el} l_{el}}} \tag{3.8}$$

In order to lighten the constrain, the CZL will have to be larger, that is, the strength will have to decrease, therefore, the strength coming from Equation 3.8 is expected to be smaller than the one of the material. It has been experienced, however, that lowering the strength of the CE will lead to a weaker global structural response and the results can be observed in Figure 3.5).

As a matter of fact, the number of the cohesive elements that span the CZL is kept constant and the CZL itself is enlarging. A significant consequence of this procedure is that the simulation predicts a fracture process zone much larger than the one which is actually occurring in reality. The improvement they obtained is therefore not measurable as highest CE mesh by CZL ratio achieved, but rather as effective length of the CE used. In this regard, by simulating a DCB test, they could use CE mesh size up to 3 mm. No mention has been done about the gains in term of CPU time.

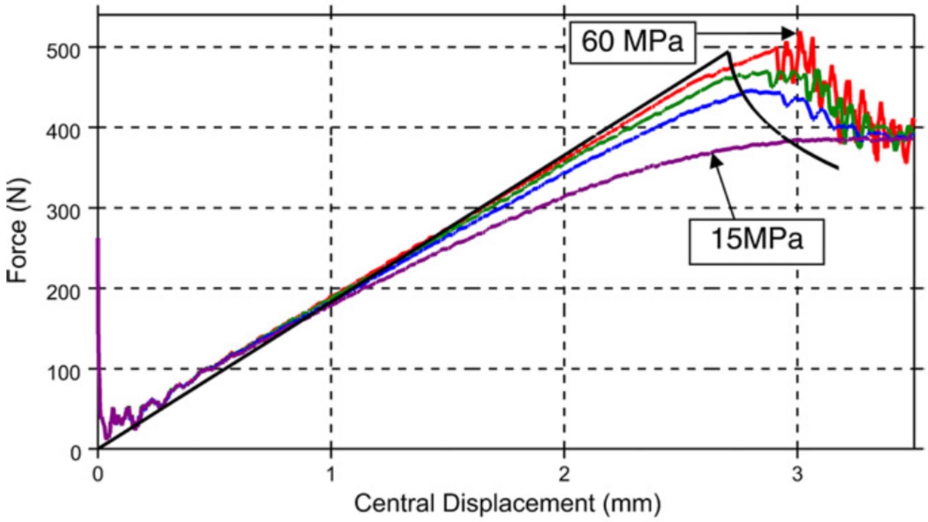

Figure 3.5: Effect of lowering the cohesive strength (Harper and Hallett, 2008).

However, the solution provided is, as suggested by the title of the article, an engineering solution, which could be very handy as a quick solution in the preliminary design phase, but it cannot be treated and considered as an effective solution to the problem because, as successively pointed out by Harper and Hallett, reducing the CE strength results in an weaker global structural response, regardless of the CE mesh size (Harper and Hallett, 2008).

3.2.3 Quadratic CEs & Integration Point

In (Álvarez et al., 2014), Alvarez et al. have introduced another type of CE, deriving from the one proposed by Camanho et al. (Camanho and Davila, 2002) which employs 6 nodes instead of 4 (Figure 3.6), meaning that quadratic shape functions could be used to interpolate the opening.

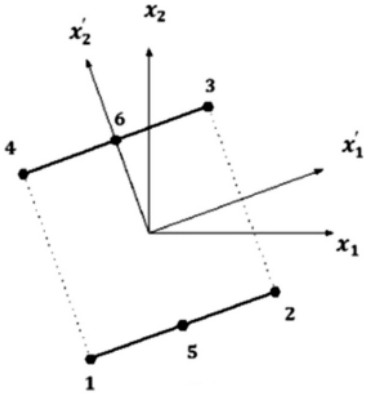

Figure 3.6: Six nodes CE (Álvarez et al., 2014).

The authors developed their own CE, introducing also the possibility to increase the number of integration points to be used (standard number is two). Good results have been achieved by employing quadratic shape functions and up to 30 integration points within the CE, using element sizes much larger than the CZL. The results can be observed in Figure 3.7:

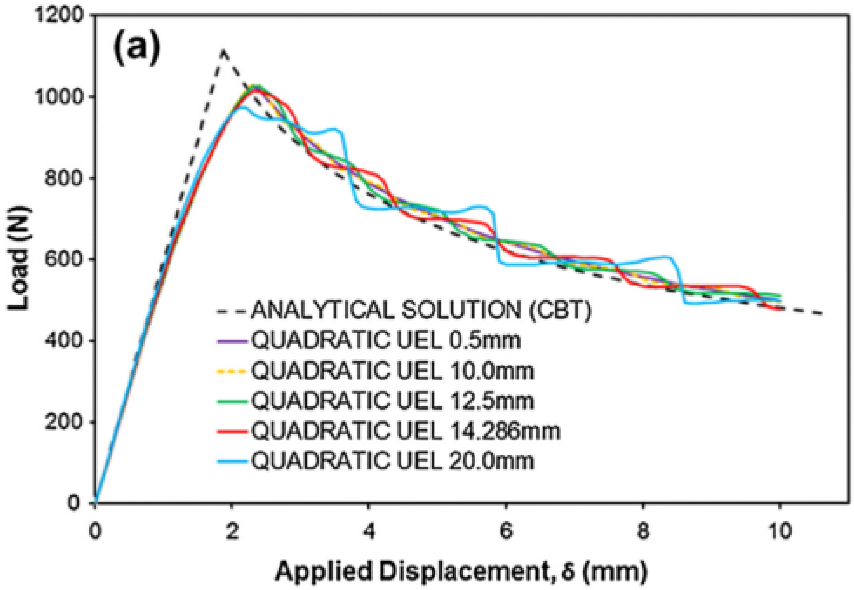

Figure 3.7: Load-Displacement curve, using 30 integration points (Álvarez et al., 2014).

The simulation of a DCB test has been carried out, and by using 30 integration points and quadratic shape functions, the results are in good agreement with the analytical curve, also for elements twice as large as the CZL, which was 10 mm. CPU time-wise they obtained a time saving of 69,5%.

3.2.4 Enriched Linear CE

Samimi, Dommelen and Geers, in (Samimi et al., 2011, 2009), developed a method to deal with discontinuity within a CE through the employment of an enrichment function used to interpolate the displacement field in the CE. Several methods can be found in literature which are able to describe discontinuities by enriching the elements belonging to the substrates, (*Floating Node Method* (Chen et al., 2014), *Augmented-FEM* (Ling et al., 2009), *Extended-FEM*(X-FEM) (Moës and Belytschko, 2002), *Phantom Node Method*(Song et al., 2006)), but few theories have been developed employing enrichment functions for CEs.

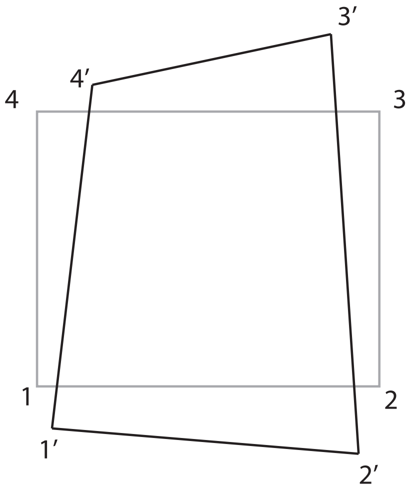

Figure 3.8: Classical deformed CE.

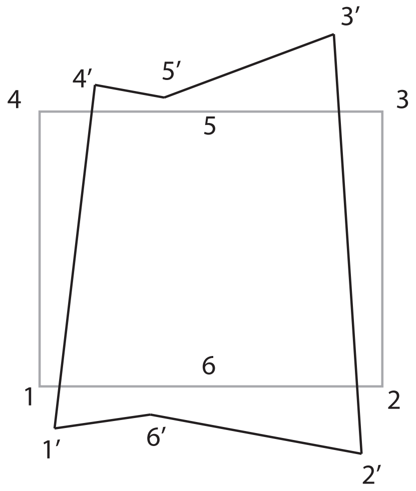

Figure 3.9: Enriched deformed CE.

The shape functions have the following form:

$$N_L = 1 - \zeta \qquad (3.9) \qquad N_R = 1 - \zeta \qquad (3.10) \qquad \Phi = \frac{1}{a}\zeta - \frac{1}{a(1-a)}\langle \zeta - a \rangle \qquad (3.11)$$

Where ζ is the a-dimensional coordinate along the top and bottom edges. The displacement field will therefore be:

$$\bar{u}_t = N_L \bar{u}_4 + N_R \bar{u}_3 + \Phi \bar{h}_t \qquad (3.12) \qquad \bar{u}_b = N_L \bar{u}_1 + N_R \bar{u}_2 + \Phi \bar{h}_b \qquad (3.13)$$

Where the vectors $\bar{u}_t$ and $\bar{u}_b$ contain the displacement fields along the top and bottom edges respectively. The vectors $\bar{h}_b$ and $\bar{h}_t$ contain the two additional d.o.f. related to nodes 5 and 6 (Figure 3.9). The last additional d.o.f. (the variable a) is present in the function used to enrich the displacement field, i.e. Φ.. The shape functions can be observed in Figure 3.10.

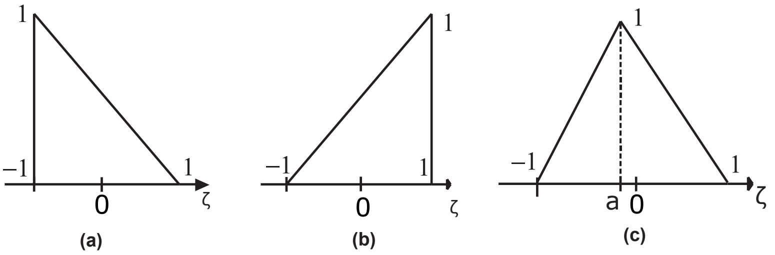

Figure 3.10: Classical linear shape functions N_L (a), N_R (b), and enriching shape function Φ (c).

The adoption of an enriched CE, implies that also the elements of the substrates must be affected from the same enrichment as well, otherwise the displacement fields between two adjacent elements is not conform.

The improvements provided by the employment of this element had to be inferred, because no explicit mention has been done either toward improvements of the maximum adoptable mesh size or time saving by applying the proposed technology to a benchmark simulation. The improvements are considerable, in fact, the number of iterations required for the enrichment CE are the 7% with respect with the standard CEs, proving a remarkable improvement in the easiness of the solution to converge.

However, regarding CE mesh size and time saving, the authors did not prove the limits of applicability of this CE. They employed a CE mesh size of 1.4 mm along the crack propagation direction. The entity of the CZL for this particular geometry has not been provided in the paper, and the only estimation which could be done is through Equation 3.4, which returns a CZL of 2.32 mm using $M^0 = 1$. Bearing in mind that this is most probably overestimated, the CE mesh size to CZL ratio is 0.60, but this estimation is likely to be underestimated.

3.2.5 Beam Theory on Elastic Foundation Solution

Another attempt to overcome the mesh size constrain has been done by Guiamatsia et al. (Guiamatsia et al., 2009, 2010). The approach they proposed consist in obtaining the analytical solution of the displacement field around the crack tip of a beam on elastic foundation meant to simulate Mode I opening and then adopt the solution as shape function (Figure 3.11). To do so, they adopted a six nodes CE, and the nodes which lie on the vertices have been enriched with the developed solution.

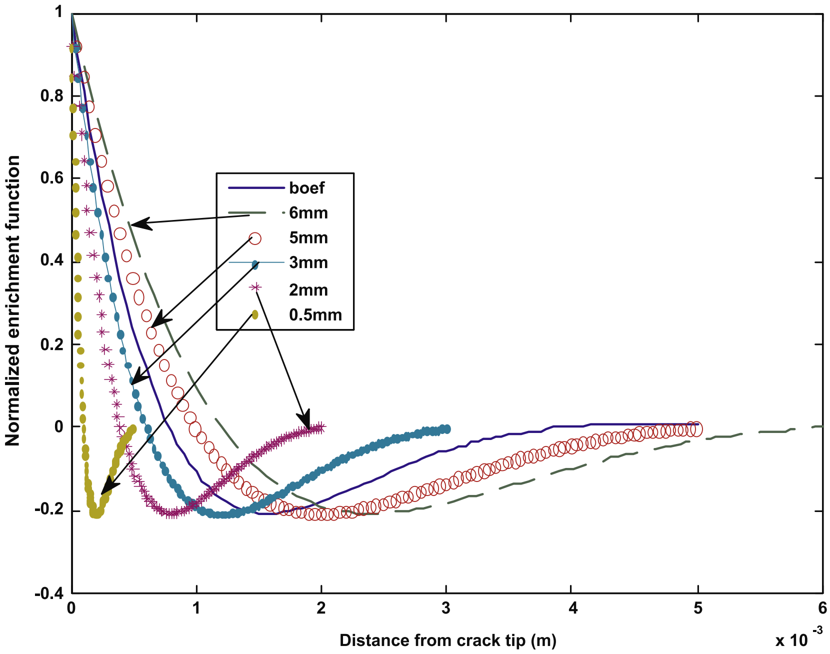

Figure 3.11: Enrichment functions implemented in the CEs (Guiamatsia et al., 2009).

The solution which they used to enrich the nodes is the following:

$$v = v_0 e^{-\beta x}[cos(\beta x) - sin(\beta x)], \qquad \beta = \sqrt[4]{\frac{K}{4EI}} \tag{3.14}$$

Where x is the distance from the crack tip, K is the elastic modulus of the foundation (K_n of the CE), E is the Young modulus and I is the moment of inertia of the beam.

Regarding the improvements obtained through this method, the CZL is not mentioned neither can be estimated, since some material properties are not reported. Time-wise, the gain is from 828 s for the 0.5 mm linear CEs, to 524 s for the proposed element, which corresponds in a time saving of 36%, while retaining the same accuracy in term of load-displacement curve of a DCB test.

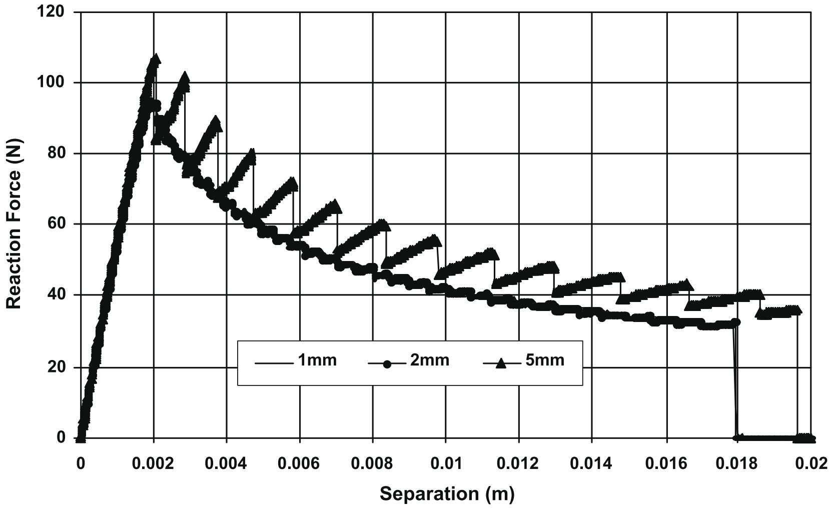

Figure 3.12: Load-displacement curve of a DCB test (Guiamatsia et al., 2009).

However, the fact that the enriching function is based on the solution obtained for a beam on elastic foundation (aiming to simulate a DCB test), restricts the field of applicability of this element to mode I simulations only.

3.2.6 Floating Node Method applied to CEs

Lu et al. enhanced the *Floating Node Method* (FNM), developed in 2014 by Chen (Chen et al., 2014), to model delamination in composite materials, by adding the adaptivity feature, and therefore creating the *Adapted-Floating Node Method* (A-FNM).

The elements created according to the FNM (Fig. 3.13) possess more degree of freedom than their standard FEA counterparts. These additional degrees of freedom are necessary to model the displacements of supplementary nodes, i.e. *Floating Nodes*, embedded in the element. The floating nodes step into play once a discontinuity (crack) must be modelled within the element. The floating nodes, so far unused and not-yet defined, find their positions in the element such as to naturally follow the crack path. Chen et al. positioned a linear CE in between the newly created substrates to adhere to the CZM technique.

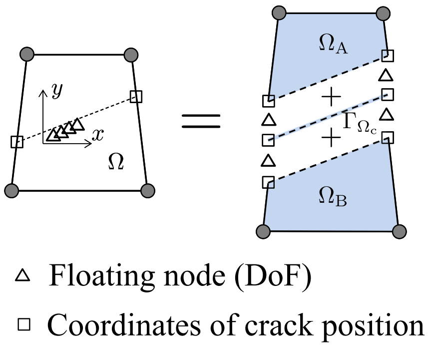

Figure 3.13: Element partitioning according to the FNM (Chen et al., 2014).

Lu et al. pushed this idea further, by introducing the possibility of the elements to adaptively partition based on the damage state of the element itself, such as to further reduce the computational time. The CL is estimated using the smallest value resulting from Eq. 3.2 and Eq. 3.4, the zone over which the enrichment with the floating nodes must be performed is establish to be three times the evaluated CZ. The refinement zone therefore advances with the crack tip, ensuring that the steep stress gradient is well captured throughout the simulation (Fig. 3.14).

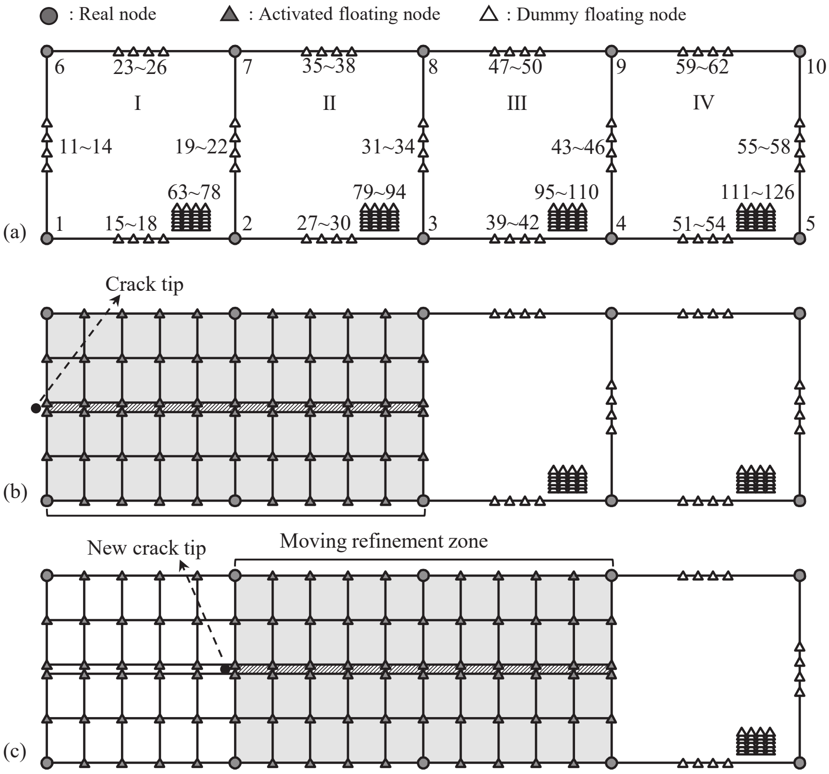

Figure 3.14: Refinement process of the A-FNM; (a) not-refined element; (b) crack initiation; (c) crack propagation (Lu et al., 2018).

The A-FNM has been verified through several tests, the DCB test being one of them, and also the most relevant to the present research. Noteworthy improvements have been achieved using this method, an original mesh size of 3 mm has been used, reduced to 0.2 mm within the refinement zone. Due to the fact that the mesh size reduces, the measurable CZ to mesh size ratio is not relevant in this case. The required CPU time for the analysis to be completed results to be 52% of the benchmarked solution using linear CEs.

Chapter 4

Proposed Solutions

Having regard to the approach other authors used to overcome the limitation of the mesh size, the author decided to conduct further investigations regarding two of the above-cited solutions: using higher order polynomials to describe the opening and adopting an adaptive integration scheme. While the former has a negative effect on the computational time, the latter could compensate, if not overcompensate, the consequences of having an additional degree of freedom for each node.

Regarding the first point, two attempts have been made: developing the analytical model of the CE using a II order polynomials and a III order polynomials. The choice of increasing the order of the functions used to interpolate the displacement field is an attempt to discretize it with equations that best suits the actual displacements experienced at the crack tip during delamination (Fig. 3.2). It must be clarified that although the II order CE is actually adopting II order polynomials to interpolate the displacement field, what we named after ”III order CE” is not using only the polynomial as shape function, but also a supplementary term, whose nature and meaning will be later assessed.

The implementation of adaptively integration schemes has been performed for the III Order CE only, because the analysis of the results coming from the II Order CE gave no reason to proceed further in decreasing the computational time related to that element.

Both the elements integrate the possibility to undergo large displacements, since an Update Lagrangian approach has been adopted, that is, the deformed configuration is used as reference to compute traction and opening. Equivalent measures to the Cauchy stress tensor and Almansi strain tensor have been employed, such as that openings and tractions have been evaluated taking into account the current local deformation of the domain.

The analytical model of the CEs has been implemented in the software *Abaqus*®. This structural solver offers the possibility to integrate user-defined elements within the library of standard elements embedded in the software. The programming language FORTRAN has been employed to create the numerical procedure. The compilation of the code and the structural analysis have been performed on the computer cluster offered by TUDelft.

This chapter will therefore present the product of the present research and will be divided in two sections, each one for a CE.

4.1 II Order CE

The II order CE has been developed in a 2D space, this choice derives from the fact that the present study does not focus on the features that only a 3D simulation can capture. This modelling choice, moreover, has been done also by many other authors due to the same reason (Samimi et al., 2011; Guiamatsia et al., 2009; Lu et al., 2018; Álvarez et al., 2014). The II Order CE can be seen in its natural reference system in Figure 4.1. It is important to clarify that, in its initial state, the edges 1-2-3 and 4-5-6 are overlapped, but, due to clarity, they are depicted as if they were opened already. The fact that the CE has initially zero thickness, leads to an impossibility to normalize the CE dimensions along the ξ direction.

Second order polynomials have been employed to describe the displacement fields of the upper and lower edges of the CE. Each node possesses two degrees of freedom, that are, the translations along the axis ξ and η. Due to the peculiar utilization of the CE, there is no need to describe the displacement field through the thickness. In fact, only the displacements of the top and bottom facets are considered, and the opening is simple computed as their relative displacement.

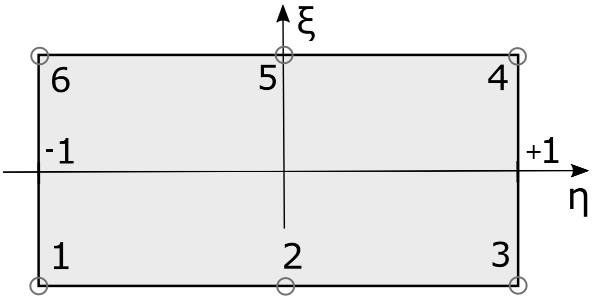

Figure 4.1: II Order CE.

Both the horizontal and vertical displacements are therefore described through the following shape functions, respectively associated with the nodes 1(6), 2(5) and 3(4):

$$N_1(\eta) = \frac{\eta(\eta-1)}{2}; \qquad N_2(\eta) = (\eta-1)(\eta+1); \qquad N_3(\eta) = \frac{\eta(\eta+1)}{2} \tag{4.1}$$

4.1.1 Computing the opening

In the case of linear CEs, the orientation of the normal and tangent vector of the mid-line is the same throughout the domain of definition of the CE. Therefore, to compute the local effective opening (in the deformed frame of reference), a simple linear mapping (rotation) should be applied to the opening evaluated in the undeformed frame of reference. Moreover, the mapping law is constant throughout the domain ($\forall \eta \in \Gamma_0$).

In case of a higher order CE, the local orientation of the mid-line varies throughout the domain. Following the definition of the mid-line, the procedure to evaluate the local angle of rotation of the domain is through a parameterization of the top and bottom deformed facets in the local undeformed frame of reference, and then obtain a parameterized description of the CE domain (Γ), from which the orientation angle can be extrapolated.

Referring to Figure 4.2, the parametrized deformed mid-line can be expressed as follows:

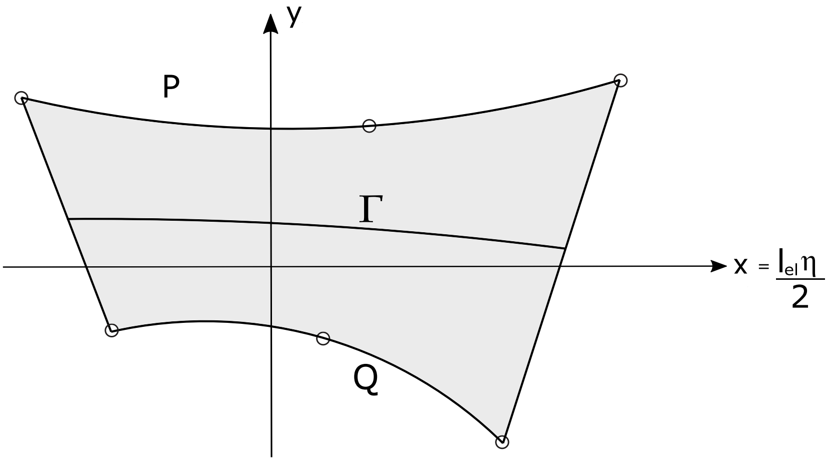

Figure 4.2: II Order Deformed CE. Emphasis on the parametrized deformed domain.

$$P(\eta) = \begin{cases} P_{x_L}(\eta) = \frac{l_{el}}{2}\eta + h_{CE_{top}}(\eta) \\ P_{y_L}(\eta) = v_{CE_{top}}(\eta) \end{cases} \tag{4.2}$$

$$Q(\eta) = \begin{cases} Q_{x_L}(\eta) = \frac{l_{el}}{2}\eta + h_{CE_{bot}}(\eta) \\ Q_{y_L}(\eta) = v_{CE_{bot}}(\eta) \end{cases} \tag{4.3}$$

$$\Gamma(\eta) = \begin{cases} \Gamma_{x_L}(\eta) = \frac{Q_{x_L}(\eta)+P_{x_L}(\eta)}{2} \\ \Gamma_{y_L}(\eta) = \frac{P_{y_L}(\eta)+P_{y_L}(\eta)}{2} \end{cases} \tag{4.4}$$

Where $h_i(\eta)$ and $v_i(\eta)$, the horizontal and vertical displacements, include the shape functions of the CE. The l_{el} is the length of the CE in the undeformed configuration. The parametrization has been performed in the local undeformed frame of reference of the CE $\{x;y\}$.

From Equation 4.4, the local angle and the $d\Gamma$ (which will be used when integration will be performed) can be evaluated as:

$$\alpha(\eta) = atan\left(\frac{\frac{\partial\Gamma_{x_L}}{\partial\eta}}{\frac{\partial\Gamma_{y_L}}{\partial\eta}}\right) \tag{4.5}$$

$$d\Gamma(\eta) = \sqrt{\left(\frac{\partial\Gamma_{x_L}}{\partial\eta}\right)^2 + \left(\frac{\partial\Gamma_{y_L}}{\partial\eta}\right)^2} d\eta \tag{4.6}$$

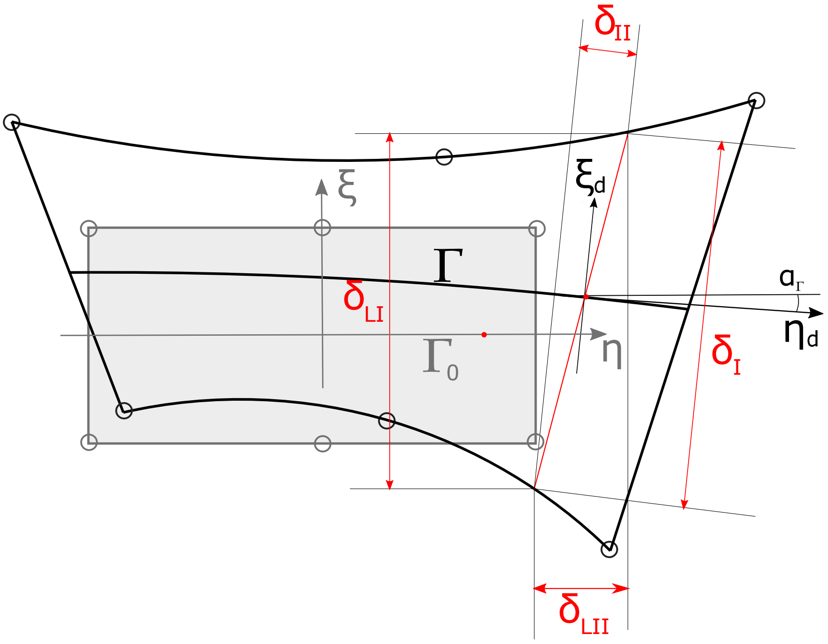

Figure 4.3: II Order Deformed CE. Emphasis on the openings in the deformed reference system.

Once the angle α_Γ has been computed, the mapping can be applied to the opening calculated in the local undeformed frame of reference $\{\xi;\eta\}$, that is, $\boldsymbol{\delta}_L$, such as to obtain the opening in the local deformed frame of reference $\{\xi_d;\eta_d\}$, that is, $\boldsymbol{\delta}$ (Figure 4.3):

$$\boldsymbol{\delta} = \begin{bmatrix} \delta_I \\ \delta_{II} \end{bmatrix} = \boldsymbol{\Phi}(\eta) \cdot \boldsymbol{\delta}_L = \begin{bmatrix} cos(\alpha_\Gamma) & sin(\alpha_\Gamma) \\ -sin(\alpha_\Gamma) & cos(\alpha_\Gamma) \end{bmatrix} \cdot \begin{bmatrix} \delta_{I_L} \\ \delta_{II_L} \end{bmatrix} \tag{4.7}$$

$$\boldsymbol{\delta}_L = \boldsymbol{b} \cdot \boldsymbol{R} \cdot \boldsymbol{u} \tag{4.8}$$

$$\boldsymbol{b}^T = \begin{bmatrix} 0 & -N_1(\eta) \\ -N_1(\eta) & 0 \\ 0 & -N_2(\eta) \\ -N_2(\eta) & 0 \\ 0 & -N_3(\eta) \\ -N_3(\eta) & 0 \\ 0 & N_3(\eta) \\ N_3(\eta) & 0 \\ 0 & N_2(\eta) \\ N_2(\eta) & 0 \\ 0 & N_1(\eta) \\ N_1(\eta) & 0 \end{bmatrix} \tag{4.9}$$

$$\boldsymbol{R} = \begin{bmatrix} \boldsymbol{r} & \dots & \boldsymbol{0} \\ \vdots & \ddots & \vdots \\ \boldsymbol{0} & \dots & \boldsymbol{r} \end{bmatrix} \tag{4.10}$$

$$\boldsymbol{r} = \begin{bmatrix} cos(\alpha_{\Gamma_0}) & sin(\alpha_{\Gamma_0}) \\ -sin(\alpha_{\Gamma_0}) & cos(\alpha_{\Gamma_0}) \end{bmatrix} \tag{4.11}$$

$$\boldsymbol{u} = \begin{bmatrix} u_1 \\ u_2 \\ \vdots \\ u_{12} \end{bmatrix} \tag{4.12}$$

Where $\boldsymbol{\Phi}(\eta)$ is the morphism (rotation) relating one reference system to the other, and it depends on the location η within the domain; $\boldsymbol{R}$ is the rotation matrix, accounting from the rotation of the CE in its undeformed configuration in the global frame of reference, whose angle is α_{Γ_0}; $\boldsymbol{u}$ is the column vector containing the variations of the degrees of freedom of the CE (nodal displacements).

4.1.2 Integration Procedure

From the Virtual Work Principle, a system in a certain physical configuration, under a certain system of forces, can be considered to be in equilibrium if, and only if, the following condition holds: the external work resulting from the application of a virtual infinitesimal system of displacements (compatible with the constraints of the system) is equal to the internal work obtained in the same way. In the case of a CE, this principle can be expressed with the following mathematical condition:

$$\int_{\Gamma} \boldsymbol{d\delta}^T \cdot \boldsymbol{\tau} d\Gamma = \boldsymbol{du} \cdot \boldsymbol{F_{ext}} \tag{4.13}$$

Where $\boldsymbol{\tau}$ is the column vector containing the traction that the element provides along the directions defined by the frame of reference $\{\xi_d; \eta_d\}$ (Figure 4.3), corresponding to mode I and mode II opening, $\boldsymbol{du}$ is the row vector containing the infinitesimal virtual and compatible variations of the degree of freedom of the CE, $\boldsymbol{d\delta}$ is column vector containing the infinitesimal virtual variation of the openings caused by $\boldsymbol{du}$, and $\boldsymbol{F}_{ext}$ is the column vector containing the nodal external forces applied to the CE's degrees of freedom.

For sake of simplicity, the two entities which must be summed through the dot product in Equation 4.13 are developed singularly and then summed up. This allows to treat every opening, and its respective traction, separately, so the whole process results to be more understandable and fluid. The variation of δ_I and δ_{II} with respect to the variation of each degree of freedom must be considered, and since the procedure for both is equal, only the development of the former entity is here presented:

$$d\delta_I = du_1 \frac{\partial \delta_I}{\partial u_1} + du_2 \frac{\partial \delta_I}{\partial u_2} + ... + du_{12} \frac{\partial \delta_I}{\partial u_{12}} = \boldsymbol{du} \cdot (\boldsymbol{\nabla} \delta_I) \tag{4.14}$$

Where ∇ is the Nabla operator. When this operator is applied to a scalar-valued function, it returns the gradient of the function in the frame of reference in which the Nabla operator is defined. In this case, the Nabla operator and the vector resulting form its application are both considered to be column vectors, containing as much elements as the number of degrees of freedom.

The formulation of the CE is somehow different from the standard element formulation, in this case the openings take the place of the strains when the internal energy must be evaluated. In FEA literature, the variation of the strain with respect to the degrees of freedom is conventionally referred to as B matrix. In case of the CEs, the same label is used, but the variations of the openings are considered instead of the strain.

From Equation 4.7, the product rule must be taken int account when processing the derivative, which will therefore be composed by two terms:

$$\boldsymbol{\nabla} \delta_I = \boldsymbol{B}_I = \Big(\boldsymbol{\nabla} \cdot \boldsymbol{\Phi_I}\Big) \cdot \boldsymbol{b} \cdot \boldsymbol{R} \cdot \boldsymbol{u} + \Big[\boldsymbol{\nabla} \cdot \Big(\boldsymbol{b} \cdot \boldsymbol{R} \cdot \boldsymbol{u}\Big)^T\Big] \cdot \boldsymbol{\Phi_I}^T \tag{4.15}$$

Where $\boldsymbol{\Phi_I}$ is the first row of the matrix $\boldsymbol{\Phi}$. In the case of δ_{II} ($\boldsymbol{B}_{II}$), the second row will be used, $\boldsymbol{\Phi_{II}}$. The formulation of Equation 4.15 has been attained by explicitly developing the derivatives in Equation 4.14 and then rearranging the terms in an implicit matrix form. It is therefore a natural consequence that the tensor-size compatibility is automatically retained.

The derivatives belonging to the first addend in Equation 4.15 have been analytically computed with the software Wolfram Mathematica®, to ensure the consistency of the analytical derivation. The procedure is presented in Appendix A. Alternatives, such as by-hand derivations or numerical evaluation of the derivatives, were discarded because a high degree of inaccuracy due to human error could affect the solution calculated by hand, and zero-finding algorithms, such as Newton-Ramphson, are much more time consuming compared to the implementation of the analytical equations. The product of the derivative of the second addend simply returns $\boldsymbol{R}^T \cdot \boldsymbol{b}^T$.

By filling Equation 4.13 with Equation 4.15:

$$\boldsymbol{du} \int_\Gamma \boldsymbol{B}^T \cdot \boldsymbol{\tau} d\Gamma = \boldsymbol{du} \cdot \boldsymbol{F_{ext}} \tag{4.16}$$

From Equation 4.16, the $\boldsymbol{du}$ can be elided, which is equivalent to state that the effects that the virtual variations of the degrees of freedom have both on the external work and the internal work are the same (linear relation) and can be therefore elided. The resulting equation is essentially a balance between external and internal forces. The vector of the internal forces, though, can be further developed . In particular, the aim here is to linearize the generically non-linear response of the internal forces of the system with respect to the variation of the degrees of freedom, around the hypothesized equilibrium configuration. Equation 4.16 is rewritten as follows:

$$\int_\Gamma \boldsymbol{B}^T \cdot \boldsymbol{\tau} d\Gamma - \boldsymbol{F_{ext}} = \boldsymbol{0} \qquad \Longrightarrow \qquad \mathscr{L}(\boldsymbol{u}) = \boldsymbol{0} \tag{4.17}$$

In this form, it is clear that the problem reduces to find the zero of the vector-valued function $\mathscr{L}$, which is dependent on n degrees of freedom. The Newton-Ramphson procedure is used to achieve that. The iterative process is exemplified, for a one dimension function, in Figure 4.4:

Given the initial guess of the solution, i.e. $\boldsymbol{u}_0$ (corresponding to a set of displacements in our case), the next solution, i.e. $\boldsymbol{u}_1$, is found through the development of the function $\mathscr{L}$ with the Taylor series, around the point $\boldsymbol{u}_0$, truncating the development at the first order (linear):

$$\mathscr{L}(\boldsymbol{u}) \approx \mathscr{L}(\boldsymbol{u}_0) + (\nabla \cdot \mathscr{L})\Big|_{\boldsymbol{u}_0} \cdot (\boldsymbol{\Delta}) \tag{4.18}$$

In 4.18, $\boldsymbol{\Delta}$ is the unknown to solve the Equation for. It represents the adjustment to apply to the previous solution during the iteration process. In Equation 4.18, a differentiation must be performed, but before proceeding, a change of variable is performed in Equation 4.17, which allows to rewrite the integral as the following:

$$\int_{-1}^{1} \boldsymbol{B}^T \cdot \boldsymbol{\tau} \Big(\nabla \boldsymbol{J} \Big) d\eta \tag{4.19}$$

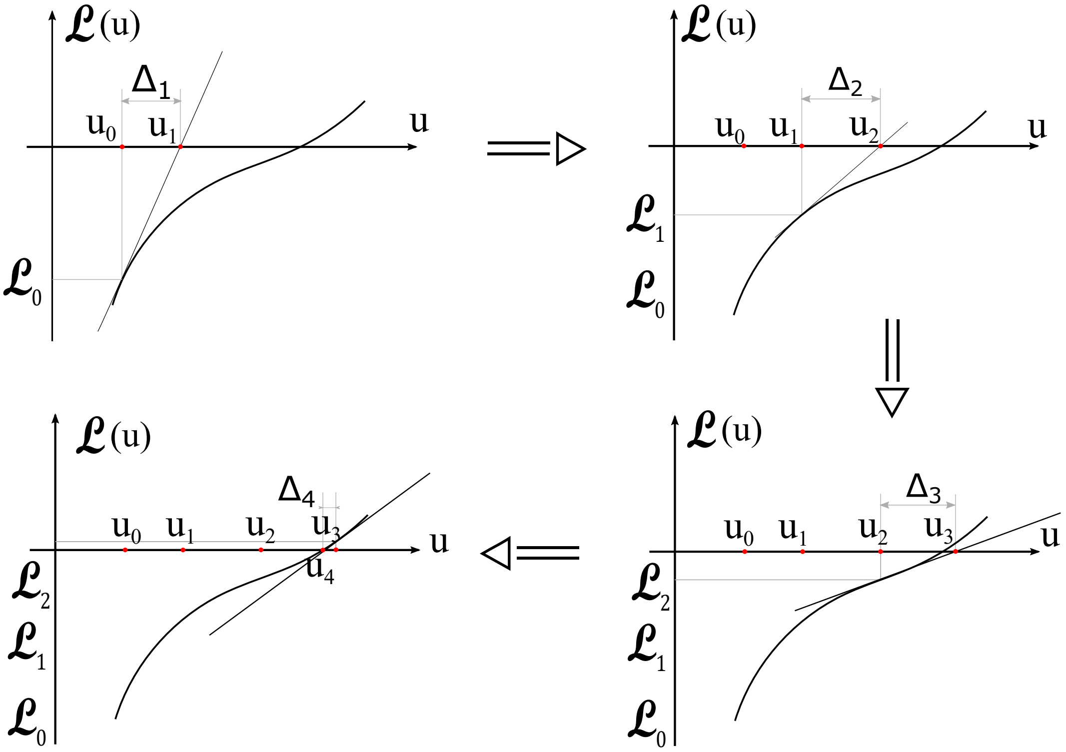

Figure 4.4: Illustration of the iterative process of finding the zero of a function.

Where $\nabla \boldsymbol{J}$ is the determinant of the Jacobian of the transformation, a scalar quantity, expressed in Equation 4.6, which represents the local infinitesimal variation of the domain Γ with respect to the variable η.

This transformation allows to perform the differentiation inside the integral, since the domain of integration is independent from the variables over which the differentiation is computed. The term $\mathscr{L}(\boldsymbol{u}_0)$ in Equation 4.18 is referred to as *residual*, and it consists of the difference between the external and the internal forces for each degree of freedom evaluated in the configuration $\boldsymbol{u}_0$. The term which deserves more attention is $\nabla \cdot \mathscr{L}$, that is, the *stiffness matrix* of the CE, also referred to as $\boldsymbol{K}$. In a single variable problem, it is equivalent to the steepness of the curve in Figure 4.4. The stiffness matrix of the element is particularly important for the scope of this research, because, besides characterizing the response of the CE, it is one of the two informations which are required to be passed to the main structural solver (Abaqus).

The other fundamental feature required from the solver is the *Right Hand Side* (RHS) vector, containing the contribution of the element to the global residual vector for each degree of freedom.

The stiffness matrix will, thus, be valuated by performing the differentiation, and the subsequent integration, of the following entity:

$$\boldsymbol{B}^T \cdot \boldsymbol{\tau}\Big(\nabla \boldsymbol{J}\Big) \tag{4.20}$$

When differentiating Equation 4.20 the chain rule must be applied, and therefore the variations of $\boldsymbol{B}$, the variation of $\boldsymbol{\tau}$ and the variation of $\nabla\boldsymbol{J}$ must be evaluated. However, it is here assumed that the variation of $\nabla\boldsymbol{J}$ and $\boldsymbol{B}$ are negligible with the respect to the variation of $\boldsymbol{\tau}$. This assumption is done because, from the beginning of the analysis, till the CE reaches the complete failure, no relevant modifications of the geometry of the CE will take place. The stress of the CE, instead, will experience non-negligible variation. Furthermore, if Quasi-Newton algorithm will be used to find the solution (the same tangent is used several times before being re-computed, see Figure 4.4), an extremely accuracy when computing the stiffness matrix is unnecessary.

If this is true for the stiffness matrix, it is not for the RHS vector. In fact, while a slightly incorrect prediction of the stiffness matrix can require more iterations to find the converged solution, an erroneous estimation of the residual (internal forces vector) may lead to diverging simulations.

Therefore, when performing the differentiation of Equation 4.20, only the variation of the traction is considered. However, since the traction is computed through Equation 2.20, if the damage variable is considered to be constant for the same reasons as above, the derivative of the traction is equivalent to the derivative of the opening, which has been defined as the $\boldsymbol{B}$ matrix. The stiffness matrix can therefore be written as:

$$\boldsymbol{K} = \int_{-1}^{+1} \left\{ \Big(1 - d_I\Big) \boldsymbol{B}_I \cdot \boldsymbol{B}_I^T + \Big(1 - d_{II}\Big) \boldsymbol{B}_{II} \cdot \boldsymbol{B}_{II}^T \right\} \Big(\nabla \boldsymbol{J}\Big) d\eta \tag{4.21}$$

While the RHS is computed as:

$$\boldsymbol{RHS} = -\int_{-1}^{+1} \left\{ \Big(1 - d_I\Big) \boldsymbol{B}_I \delta_I + \Big(1 - d_{II}\Big) \boldsymbol{B}_{II} \delta_{II} \right\} \Big(\nabla \boldsymbol{J}\Big) d\eta \tag{4.22}$$

Since the solver of ABAQUS uses the form $\boldsymbol{\Delta} = \boldsymbol{K}^{-1} \cdot \boldsymbol{RHS}$ to compute $\boldsymbol{\Delta}$, there is a minus in front of the integral because the term $\mathscr{L}(\boldsymbol{u}_0)$ in Equation 4.18 changes its sign when going from the right to the left hand side of the Equation. In the development of Equations 4.21 and 4.22, two damage variables have been considered, one for each opening mode. Although the actual value of the damage variable is unique for the CE and it is computed with Equation 2.19, using two separate damage variable is handful in case damaged CEs must act such as to prevent penetration between the two substrates ($\delta_I < 0$), therefore the response in mode I must not be affected by any damage.

For every CE an array has been stored, containing the values of the damage variables, evaluated with Equation 2.19, at thirty locations. The reason to store this values is to ensure that the damage is monotonically increasing in the CE. If, during the simulation, the damage estimated in the current converged increment is smaller than the stored value, then the latter is used to fill Equations 4.22 and 4.21. Instead, if the damage in the current converged increment is larger than the stored valued, the former is used in the integration and the stored value of the damage variable is updated.

The choice of probing the damage variable is so many points derives from the fact that a high degree of precision is required in this step. An alternative solution would have been to store the information of the analytical distribution of the damage variable within the CE. However, in case the current damage function was larger than the stored one only in a sub-domain of the CE, additional information should be stored such as to define two different damage distributions, each in a sub-domain, plus the information regarding the partitioning of the CE. The amount of data to be stored increases with the number of sub-domain created, and it is impossible to know beforehand the number of information required for the whole simulation. However, in the environment in which this research has been developed (*FORTRAN*), the length of the arrays passed to the subroutine is fixed. An alternative solution might have been found, but for the scope of this research, the described procedure has been considered satisfactory.

The integration is then numerically performed. This has been done by evaluating the integrating function in Equation 4.21 and 4.22 at several points, also known as *Integration Points* (IP), and then by operating a weighted summation over all the obtained values. The locations of the IPs are coincident with the locations where the damage has been evaluated, so as to save computational time, which means thirty IPs have been employed. The positions of the IP have been determined as roots of the Legendre polynomial (see Appendix B). Before considering the development of an adaptive integration scheme for this CE, a feasibility study has been conducted. The results, presented in the next chapter, did not justify the adoption of an adaptive integration scheme, rather they made the research turn toward the employment of even higher order shape function to interpolate the displacements and the openings.

4.2 III Order CE

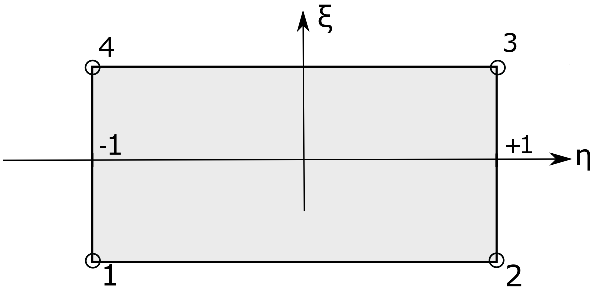

Figure 4.5: III Order CE.

The development of the III Oder CE follows the same procedure adopted for the the II Order CE. However, some differences between the two elements are present, and they will be pointed out in this section.

The only element offered by ABAQUS, which is characterized by third order shape functions, and that can be coupled with a 2D CE, is the Euler beam element. Some of the choices and subsequent decision have been made considering that the beam elements has to be used. In fact, the shape functions of the CE, initially implemented as purely third order, had to be adapted to accommodate the mismatch between beam nodes and CE nodes, due to the presence of the thickness of the beam.

The representation of the III Order CE can be observed in Figure 4.5. The first thing which can be noted is that only four nodes are used, however, every node possesses three degrees of freedom, two translational and one rotational degree of freedom. The shape functions used for the Euler beam element are presented in Equations 4.23, 4.24 and 4.25, and they describe the displacement field of the neutral axis of the beam:

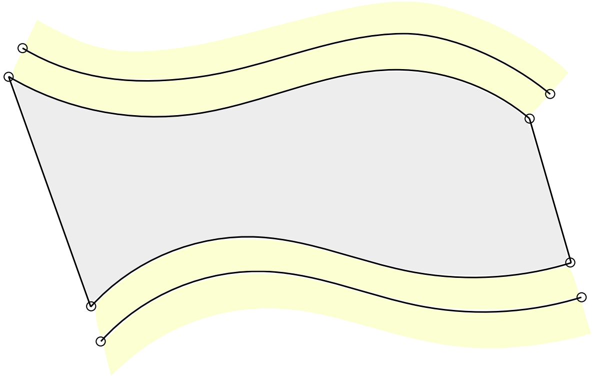

Figure 4.6: Configuration of the III Order CE between two Beam Elements.

$$\begin{cases} N_1^v(\eta) = \frac{1}{4}\Big(2 - 3\eta + \eta^3\Big) \\ N_2^v(\eta) = \frac{l_{el}}{8}\Big(1 - \eta - \eta^2 + \eta^3\Big) \\ N_3^v(\eta) = \frac{1}{4}\Big(2 + 3\eta + \eta^3\Big) \\ N_2^v(\eta) = \frac{l_{el}}{8}\Big(- 1 - \eta + \eta^2 + \eta^3\Big) \end{cases} \tag{4.23}$$

$$\begin{cases} N_1^\theta(\eta) = \frac{3}{2l_{el}}\Big(- \eta + \eta^2\Big) \\ N_2^\theta(\eta) = \frac{1}{4}\Big(- 1 - 2\eta + 3\eta^2\Big) \\ N_3^\theta(\eta) = \frac{3}{2l_{el}}\Big(\eta - \eta^2\Big) \\ N_4^\theta(\eta) = \frac{1}{4}\Big(- 1 + 2\eta + 3\eta^2\Big) \end{cases} \tag{4.24}$$

$$\begin{cases} N_1^h(\eta) = \frac{1}{2}\Big(1 - \eta\Big) \\ N_2^h(\eta) = \frac{1}{2}\Big(1 + \eta\Big) \end{cases} \tag{4.25}$$

The vertical and horizontal displacement fields of the beam (N^v and N^h) are described through third and first order polynomials respectively; the rotational displacement field (N^θ), instead, being equal to the derivative of the vertical displacement, is described by a second order polynomial. However, the Equations 4.23, 4.24 and 4.25 refer to the neutral axis of the beam, while the CEs nodes are offsetted from the neutral axis by half the beam thickness (Figure 4.6). Further functions are used to take into account this mismatch. The correlation between the displacement of the neutral axis of the beam and the displacement of the bottom and top surfaces of the CE is the following:

$$\begin{cases} h_{CE_t}(\eta) = h_{B_t}(\eta) - \frac{t}{2}\sin\theta_{B_t} \\ v_{CE_t}(\eta) = v_{B_t}(\eta) + \frac{t}{2}(1 - \cos\theta_{B_t}) \end{cases} \tag{4.26}$$

$$\begin{cases} h_{CE_b}(\eta) = h_{B_b}(\eta) + \frac{t}{2}\sin\theta_{B_b} \\ v_{CE_b}(\eta) = v_{B_b}(\eta) - \frac{t}{2}(1 - \cos\theta_{B_b}) \end{cases} \tag{4.27}$$

Where the first subscript indicates whether the displacement is referred to the CE or the beam element. The second subscript indicates whether the displacement is referred to the top or bottom CE/beam element. The thickness of the beam element is t, and θ_B refers to the rotational degree of freedom of the beam.

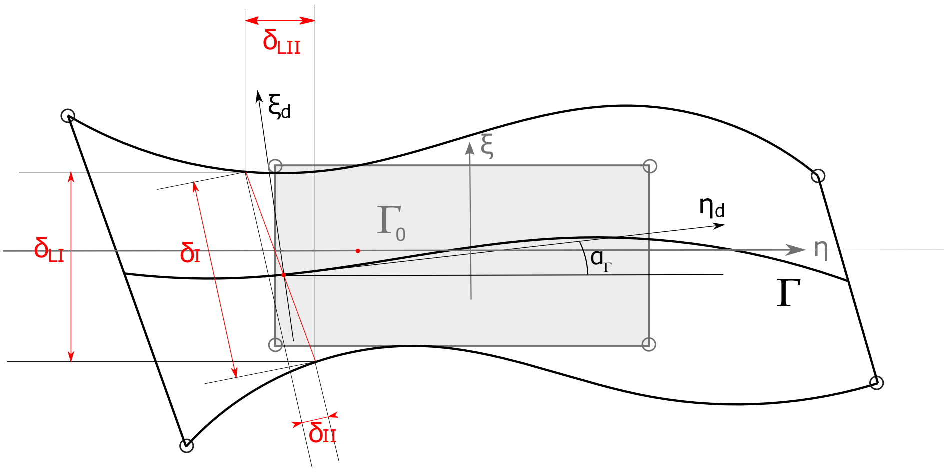

Figure 4.7: Deformed III Order CE.

4.2.1 Computing the opening

The procedure to compute the opening follows the same steps as in the II order CE, however, a modification must be done accounting for the rotation-induced extra displacement. The deformed III Order CE is pictures in Frigure 4.7.

The effective openings are evaluated as in Equation 4.7, but the local opening, $\boldsymbol{\delta}_L$ is computed as follows:

$$\boldsymbol{\delta}_L = \boldsymbol{b} \cdot \boldsymbol{R} \cdot \boldsymbol{u} + \boldsymbol{\delta}_R \tag{4.28}$$

$$\boldsymbol{\delta}_R = \frac{t}{2} \begin{bmatrix} 2 - \cos(\theta_{B_t}) - \cos(\theta_{B_b}) \\ \sin(\theta_{B_t}) + \sin(\theta_{B_b}) \end{bmatrix} \tag{4.29}$$

$$\boldsymbol{b}^T = \begin{bmatrix} 0 & -N_1^h(\eta) \\ -N_1^v(\eta) & 0 \\ -N_2^v(\eta) & 0 \\ 0 & -N_2^h(\eta) \\ -N_3^v(\eta) & 0 \\ -N_4^v(\eta) & 0 \\ 0 & N_2^h(\eta) \\ N_3^v(\eta) & 0 \\ N_4^v(\eta) & 0 \\ 0 & N_1^h(\eta) \\ N_1^v(\eta) & 0) \\ N_2^v(\eta) & 0 \end{bmatrix} \tag{4.30}$$

Therefore, the matrix $\boldsymbol{B_i}$ will be:

$$\boldsymbol{B}_i = \left(\boldsymbol{\nabla} \cdot \boldsymbol{\Phi_i}\right) \cdot \left(\boldsymbol{b} \cdot \boldsymbol{R} \cdot \boldsymbol{u} + \boldsymbol{\delta}_R\right) + \left[\boldsymbol{R}^T \cdot \boldsymbol{b}^T + \left(\boldsymbol{\nabla} \cdot \boldsymbol{\delta}_R^T\right)\right] \cdot \boldsymbol{\Phi_I}^T \tag{4.31}$$

4.2.2 Adaptive Integration Scheme

In the case of the III Order CE, an adaptive Gaussian integration scheme has been adopted, such that whenever a deeper degree of accuracy is required (crack passing through the CE) the number of integration points increases from 3 to 30 (Figure 4.8).

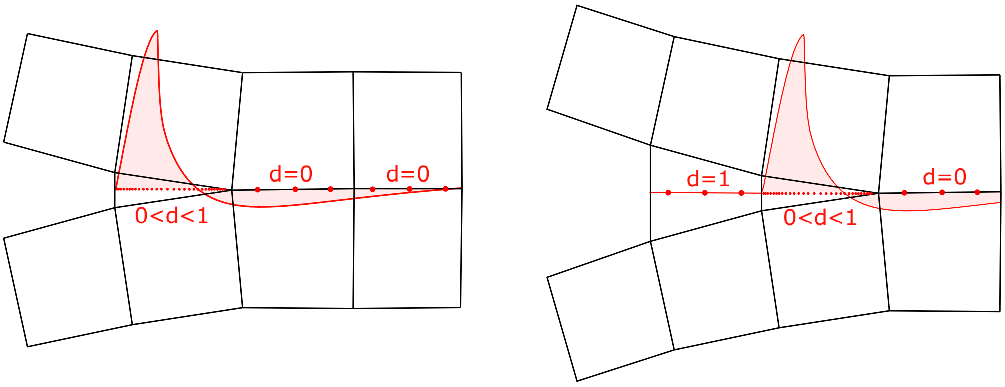

Figure 4.8: Adaptivity Gaussian integration schemes. The red dots indicate the IPs.

The weights and location of the three integration points in the domain are presented in Table 4.2.2. In case the element is not damaged, or it is fully damaged, the CE adopts three integration points throughout the domain. In case the element is partially damaged, the number of integration points is switched to 30, such as to properly catch the stress sever stress gradient. The weights and positions of the 30 IP can be found in the Appendix B.

IP #	η_{IP}	**weight**
1	$-\sqrt{3/5}$	$5/9$
2	0	$8/9$
3	$\sqrt{3/5}$	$5/9$

Table 4.1: Positions and weights of a 3 IP Gaussian scheme.

Before each iteration, the openings of the CE are preprocessed such as to establish whether 3 or 30 IPs must be used. The openings and the respective damage variables are evaluated at the same locations of the 30 IPs using the steps in Equations 2.12 to 2.20. Adopting this locations to check the status of the CE is a convenient choice, in fact, in case the element is partially damaged, the evaluation of the damage at the IP must not be carried out again if the results of the preprocessing were stored. In case the element results to be undamaged or fully damaged, no further damage variable must be computed at the location of the 3 IPs, resulting in a CPU-time saving.

The evaluations of the stiffness matrix and the right hand side vector have been performed through Equations 4.21 and 4.22 respectively.

Chapter 5

Verification and Validation

In this chapter, the methodologies that have been adopted to validate and verify the developed CEs will be presented. The first section will introduce the benchmark that have been produced using the linear CEs, such as to perform a comparison afterward. The second and third section will focus on the results obtained by employing II order CEs and III order CEs respectively.

The aim of this chapter is to analyze the correctness of the solution that has been produced by implementing the developed CEs; this can be done in two ways: by comparing the response of the new element with the one already implemented in Abauqs (linear CE), or by confronting the same response with the experimental data coming from physical tests. The former takes the name of *validation* and the latter is referred to as *verification*.

Several tests are used in industrial best practice to induce a certain fracture mode at the crack tip. In this regard, the aim of this phase of the research was to test the performances of the CE under mode I, mode II and mixed mode opening. The respective tests that have been chosen are the *Double Cantilever Beam* (DCB), *End-Notch Flexure* (ENF) and *Mixed-Mode Bending* (MMB). The set-up of these three tests have been summarized by Reeders in (Krueger, 2015).

The geometries of the simulated specimens and the material mechanical properties have been taken from (Turon et al., 2010) (ENF and MMB) and (Turon et al., 2007) (DCB). In these papers, Turon et al., present the results for the three tests that have been decided to simulate in terms of global load-displacement relation. While the DCB and ENF emulate pure mode I and mode II opening, for the MMB case the mixity mode ration must be chosen beforehand. In the above cited paper, they simulate 20%, 50% and 80% MMB tests, whereas, for the present work, it has been decided to simulate only 50% MMB test.

The standard CE used for the simulations (COH2D4) are characterized by a bilinear cohesive law; a quadratic stress criterion has been employed to determine the crack onset condition, while an energy-base criterion is used to characterize the crack growth phase, in particular, the Benzaggah-Kenane criterion (Benzeggagh and Kenane, 1996).

The features used to quantify the improvements of the solutions presented in Section 3.2 were the maximum achievable mesh size while retaining an acceptable degree of accuracy, and the computational time gain. In this Chapter the same methodology will be used.

5.1 Benchmark DCB

For the creation of the DCB benchmark, the paper (Turon et al., 2007) has been used as reference, and the same specimen has been modelled. The dimensions of the specimen are pictured in Figure 5.1.

The DCB specimen has been modeled using plain strain elements (CPE4) for the composite substrates, and standard cohesive elements have been used for the cohesive layer (COH2D4). Reduced integration option has been discarded so to avoid hourglass effect. The specimen has been modeled as one unique part, and then a partitioning has been performed such as to assign different element types and material properties. By doing so, it has been ensured that the cohesive layer and substrates share the same nodes. Five partitions have been created, and they can be seen in Figure 5.2 (the CE have initially zero thickness).

Five plain strain elements have been used through the thickness for each arm. Several mesh sizes have been adopted along the crack propagation direction, ranging from 0.01 mm to 2.5 mm. Out-of-plane thickness has been assigned to the whole model with the value of one. The material properties and the cohesive properties can be seen in Table 5.1. The same penalty stiffness has been implemented for the two opening directions.

In order to simulate zero-thickness CEs, once the mesh has been generated, it has been manually modified such that the top and the bottom rows of nodes on the CEs would have the same coordinates.

The deflection has been generated through an enforced vertical displacement at the most top/bottom left nodes of the specimen. The right surface of the specimen has been tied with zero applied displacement along the in plane directions (Figure 5.3).

Regarding the solver options (step settings), for the DCB case quasi-Newton approach has been used. When the CEs are added to the model, it is often necessary to modify the General Solution Controls of the solver. The modifications which have been applied can be checked in the input files added to the appendix of this document (see Appendix C).

The adoption of a refined mesh size of 0.0125 mm, allowed to estimate the CZL of this particular set-up to be 0.84 mm (Figure 5.4).

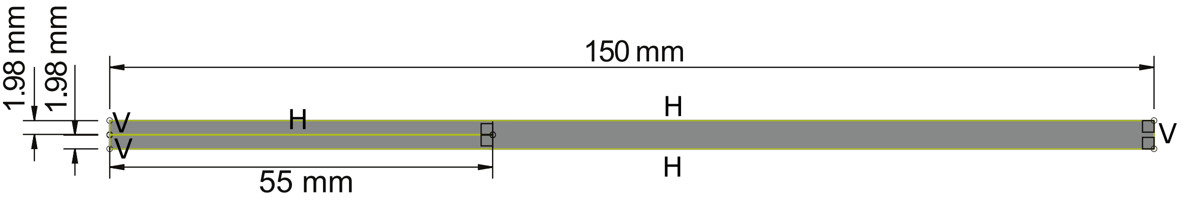

Figure 5.1: DCB geometry.

Figure 5.2: DCB partitions.

Young Modulus along fiber direction, E_{11}, [GPa]	150
Young Modulus along the orthogonal fiber direction, E_{22}=E_{33}, [GPa]	11
Shear Modulus along 1-2 and 1-3 directions, G_{12}=G_{13}, [GPa]	6
Shear Modulus along 2-3 direction, $G_{23}, [GPa]$	3.7
Poisson ratio along 2-3 direction, ν_{23}	0.25
Poisson ratio along 1-2 and 1-3 directions, ν_{12}=ν_{13}	0.45
Mode I Fracture Toughness, $G_{I,c}$, $[\frac{N}{mm}]$	0.325
Mode II/III Fracture Toughness, $G_{II,c} = G_{III,c}$, $[\frac{N}{mm}]$	1.002
Penalty Stiffness, K, $[\frac{MPa}{mm}]$	555555
Mode I Crack onset stress, τ_I^0, [MPa]	60
Mode II/III Crack onset stress, τ_{II}^0=τ_{III}^0, [MPa]	101.2
Benzeggagh-Kenane material parameter, μ	2

Table 5.1: Material and Cohesive Properties used to simulate the DCB.(Turon et al., 2007)

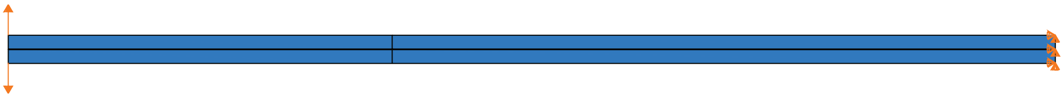

Figure 5.3: Set of BCs applied to the DCB specimen.

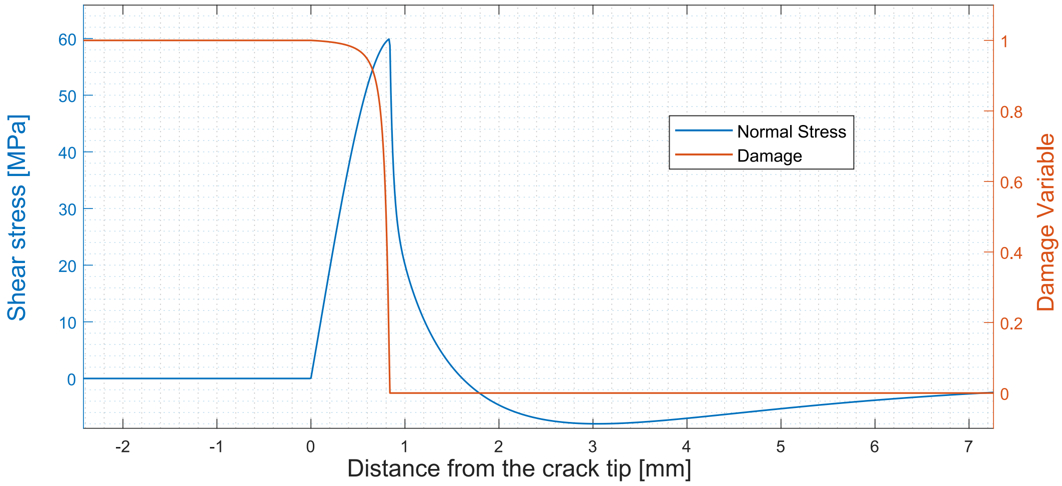

Figure 5.4: Normal stress and damage variable along the crack path for the DCB test.

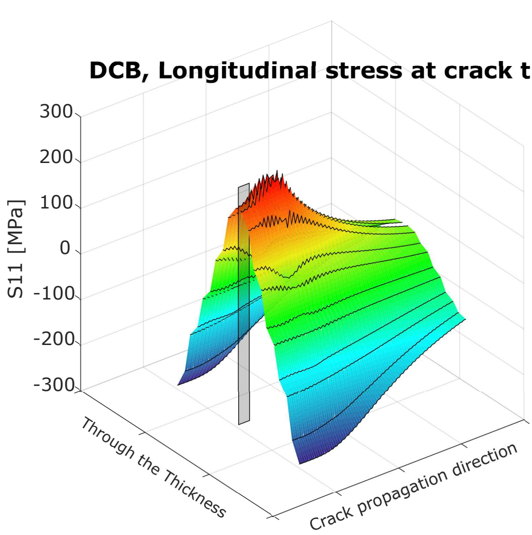

Figure 5.5: Longitudinal stress at crack tip, DCB.

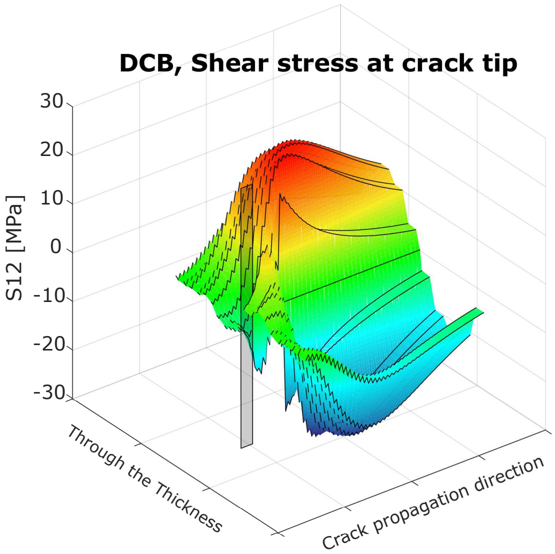

Figure 5.6: Shear stress at crack tip, DCB.

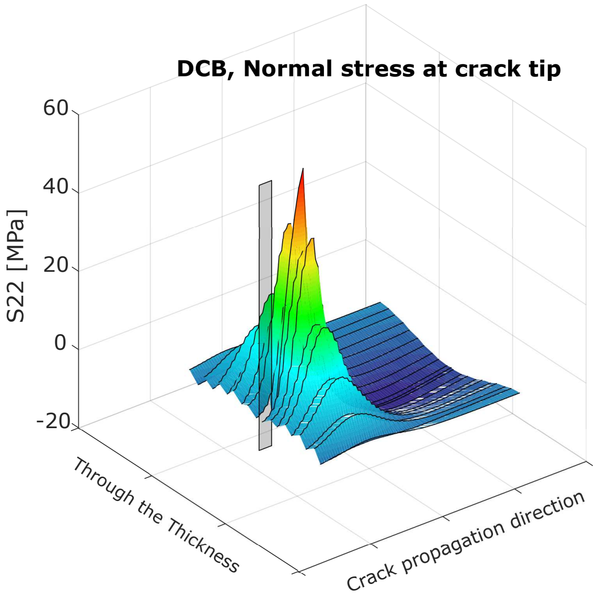

Figure 5.7: Normal stress at crack tip, DCB.

The gray planes in Figures 5.5, 5.6 and 5.7 represent the crack extension. These figures give an overview of the stress distribution around the crack tip once the fracture process zone is fully developed.

5.2 Benchmark MMB

For the creation of the MMB benchmark, the model in (Turon et al., 2010) has been simulated. Dimensions and geometry are depicted in Figure 5.8 and 5.9. In this case also the model has been partitioned.

As suggested in (Krueger, 2015), the mixed mode loading has been achieved by simulating the whole apparatus which is used to obtain a mixed mode loading condition. The leverage has been modelled as a discrete rigid 2D part, R2D2 (Figure 5.9). As discussed in (Turon et al., 2010; Krueger, 2015), the mixed mode loading ratio can be tuned by changing the length c (Figure 5.9). In this case, 50% MMB is simulated, corresponding to a length of 63.18 mm.

The elements used for the cohesive layer and the substrates are the same which have been used for the DCB benchmark (CPE4-COH2D4), however, the material is different. The material properties are listed in Table 5.2.

Regarding the mesh, 10 elements have been used through the thickness for each one of the composite arms. In the already cracked substrates partitions, 3 mm wide elements have been used, while in the other partitions the elements are 0.1 mm wide. Every element has a 1 mm out-of-plane thickness. While in the DCB and ENF cases the limit of maximum adoptable mesh size has been tested by using a progressively increasing mesh size, in this case the 0.1 mm CE mesh size already produced inconsistent results with the respect to the analytical curve (see Figure 5.25), therefore, no investigation on the maximum mesh size has been conducted.

In the paper (Krueger, 2015), it has been suggested to create an interaction between the two parts by linking the most bottom-left node of the leverage with the most top-left node of the specimen through a multi point constraint. However, due to a gap between these two nodes, generated by numerical inaccuracy, the applied constrain has been defined through equations, and the in-plane displacements of the two nodes have been coupled with two separate equations expressing the displacement constrain.

In the same paper it has been advised to use a multi point constraint between the middle arm of the leverage and the top surface of the composite, which would constrain the end of the arm to lie on the surface. However, this type of constrain could not be found in the software used (ABAQUS). Therefore, a different modeling technique has been used: a surface to surface contact has been applied, using the top specimen surface as master surface, and node of the leverage as a slave surface. Hard type of contact has been used as normal contact property and frictionless contact has been employed for tangential contact property definition.

As showed in Figure 5.11,the CZL for the MMB case was found to be 1.8 mm.

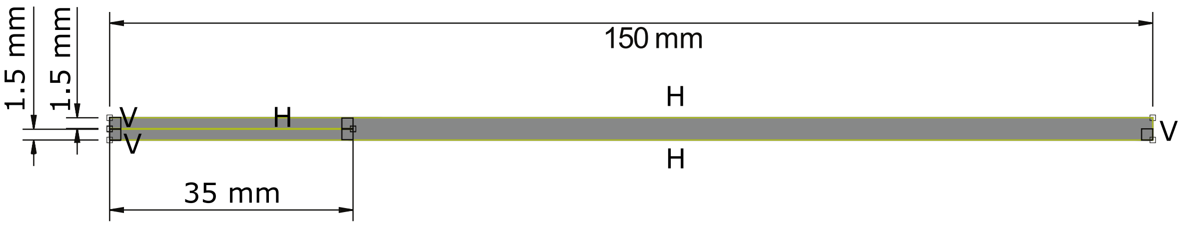

Figure 5.8: MMB geometry.

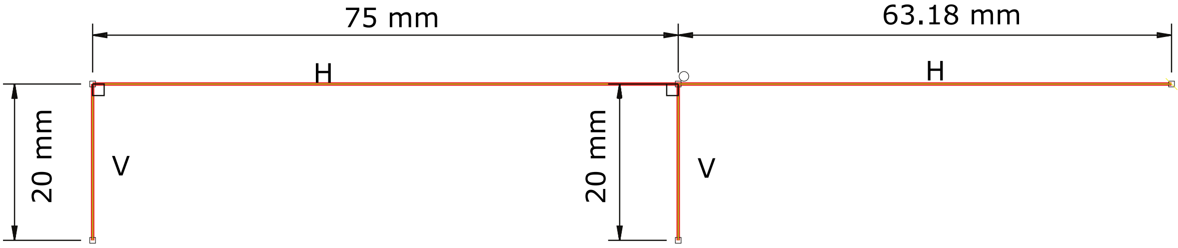

Figure 5.9: Lever Geometry.

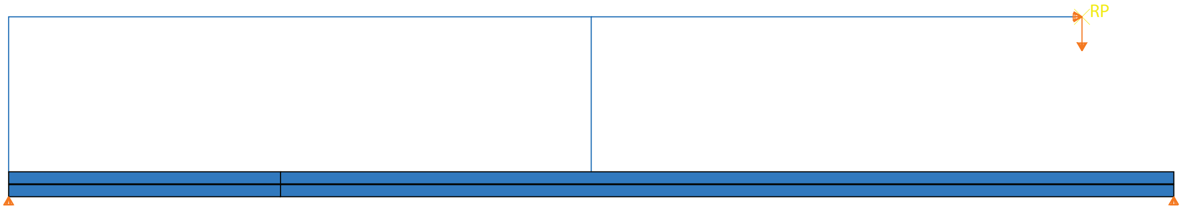

Figure 5.10: MMB load and BCs.

Young Modulus along fiber direction, E_{11}, [GPa]	120
Young Modulus along the orthogonal fiber direction, E_{22}=E_{33}, [GPa]	10.5
Shear Modulus along 1-2 and 1-3 directions, G_{12}=G_{13}, [GPa]	5.25
Shear Modulus along 2-3 direction, G_{23}, $[GPa]$	3.48
Poisson ratio along 2-3 direction, ν_{23}	0.3
Poisson ratio along 1-2 and 1-3 directions,ν_{12}=ν_{13}	0.5
Mode I Fracture Toughness, $G_{I,c}$, $[\frac{N}{mm}]$	0.26
Mode II/III Fracture Toughness, $G_{II,c} = G_{III,c}$, $[\frac{N}{mm}]$	1.002
Penalty Stiffness, K, $[\frac{MPa}{mm}]$	555555
Mode I Crack onset stress, τ_I^0, [MPa]	30
Mode II/III Crack onset stress, τ_{II}^0=τ_{III}^0, [MPa]	58.9
Benzeggagh-Kenane material parameter, μ	2

Table 5.2: Material and Cohesive Properties used to simulate the DCB.Turon et al. (2010)

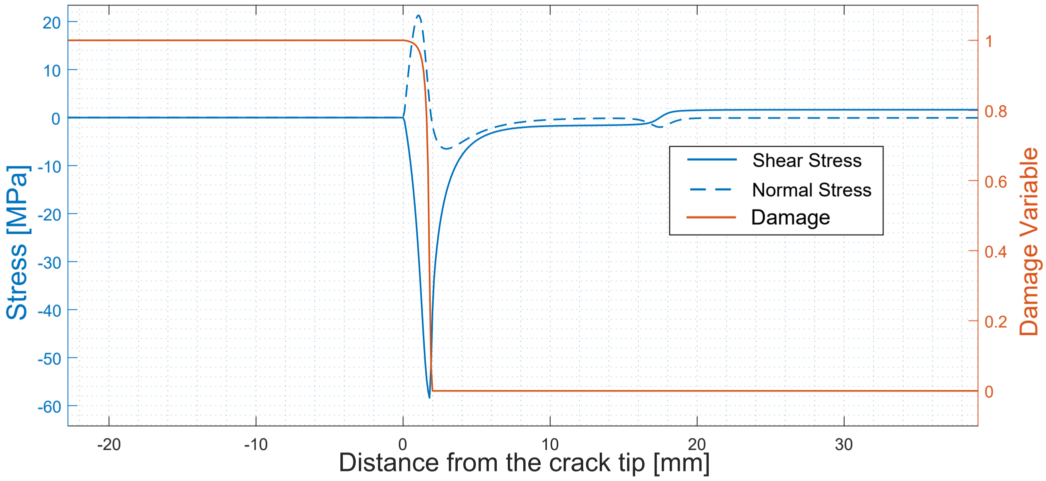

Figure 5.11: Normal stress, shear stress and damage variale along the crack path for the MMB test.

A crucial feature can be extracted in Figure 5.11. It can be noticed that the absolute value of the peak of the normal stress and the one of the shear stress measure 22 N and 58 N respectively. Since the onset stresses for mode I and mode II are 30 N and 58.9 N, it is obvious that the opening mode at the crack tip is not 50% mixed, but rather close to be 100% mode II.

Similar findings have been presented by Turon et al. in (Turon et al., 2010), where they indicate that the mixed mode opening for a point initially far from the crack tip, varies with the crack getting closer, while the test set-up is meant to induce 50% mixed mode opening throughout the simulation.

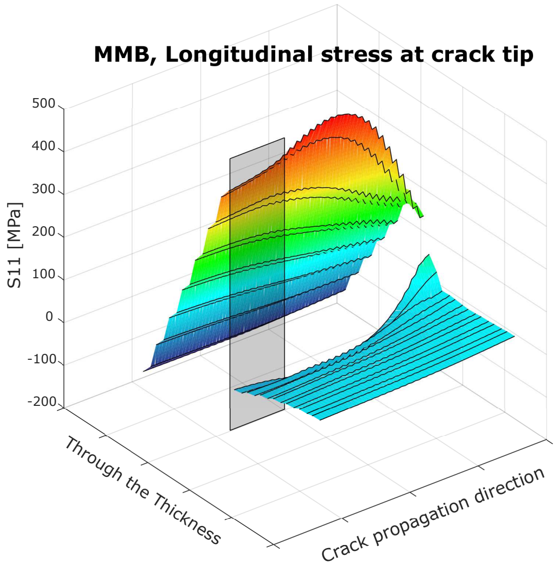

Figure 5.12: Longitudinal stress at crack tip, MMB.

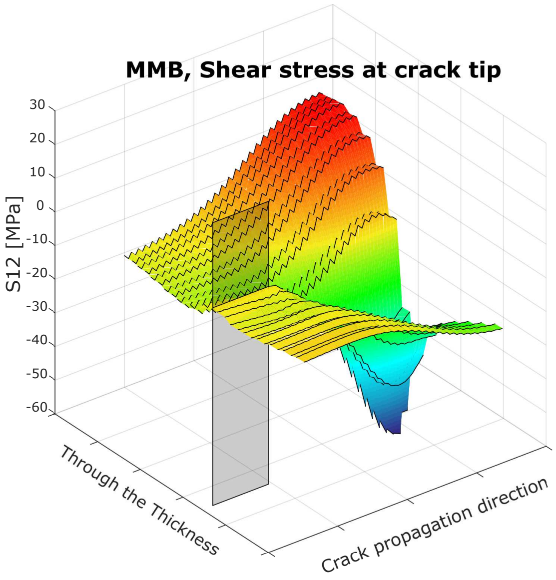

Figure 5.13: Shear stress at crack tip, MMB.

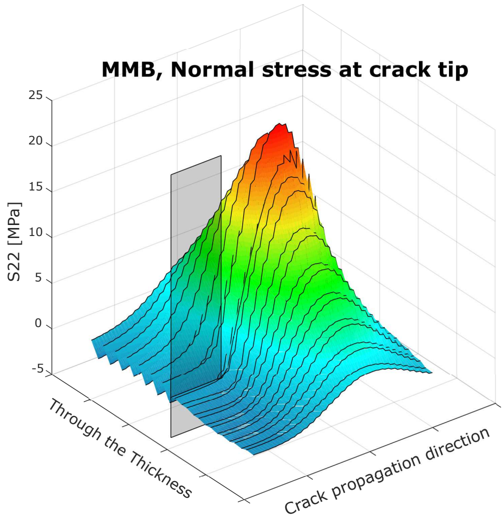

Figure 5.14: Normal stress at crack tip, MMB.

5.3 Benchmark ENF

The ENF has been simulated by following the reference in (Turon et al., 2010). This study case implements the same characteristic of the MMB test, that are: geometry, material, solver options and partitions. However, the rigid element has not been included, as the rigid loading frames are not used.

Figure 5.15: ENF Boundary Conditions.

The ENF simulation has been assessed though an applied displacement at the center of the specimen (Figure 5.15). In order to avoid the two pre-cracked substrates to penetrate each other, a surface to surface interaction (hard contact and frictionless) has been added between the two surfaces of the specimen.

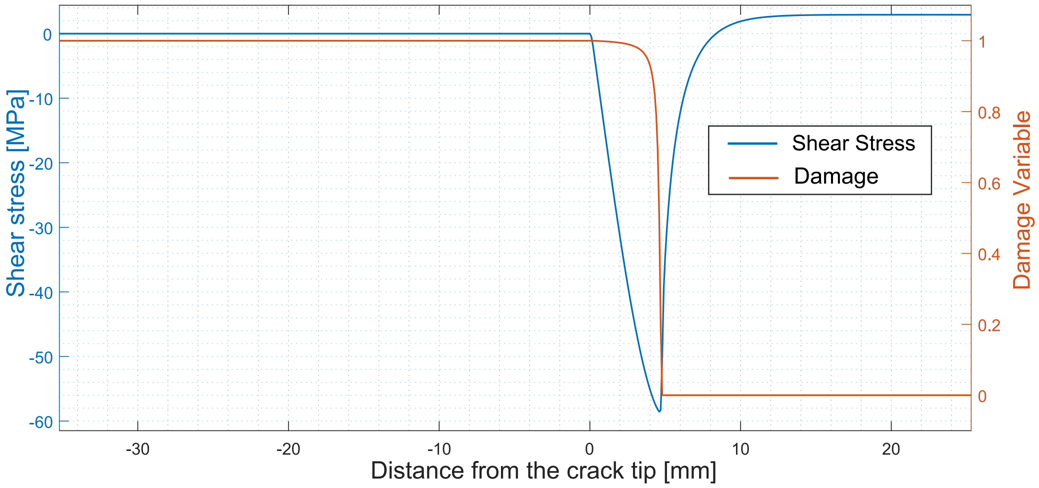

Figure 5.16: Shear stress and damage variable along the crack path for the ENF test.

From Figure 5.16, a CZL of 4.8 mm has been extrapolated.

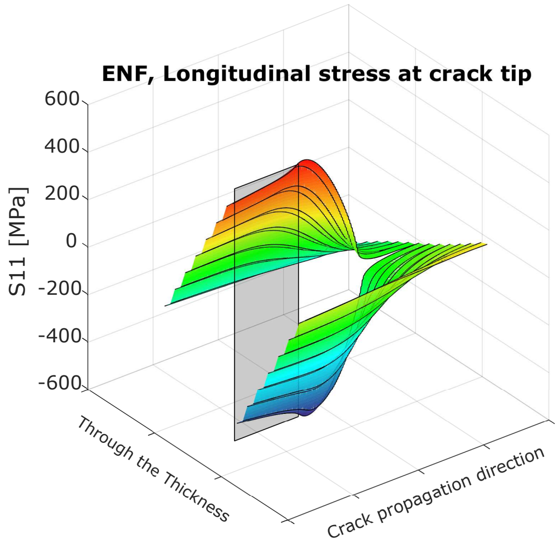

Figure 5.17: Longitudinal stress at crack tip, ENF.

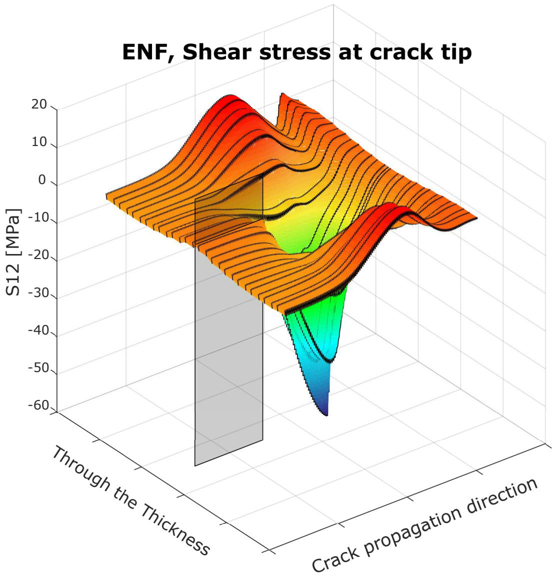

Figure 5.18: Shear stress at crack tip, ENF.

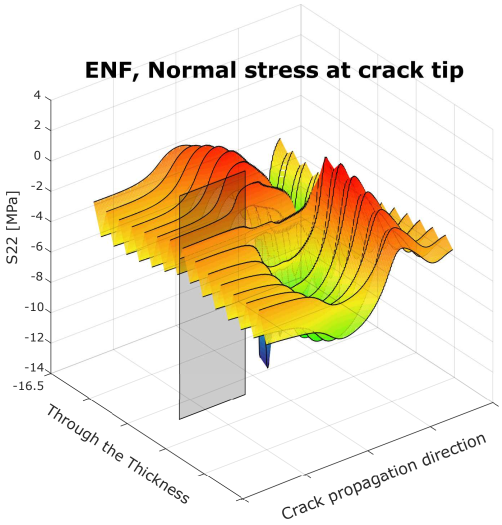

Figure 5.19: Normal stress at crack tip, ENF.

5.4 II Order CEs DCB

The model used to implement the II Order CEs is the same that has been used to simulate the DCB specimen using standard CEs (Section 5.1). Same material properties and geometries have been adopted, however, due to the compatibility which must hold between the substrates and the cohesive elements (sharing the same nodes), CPE8 elements have been used for the substrates. These elements have one node for each vertex and another one for each edge, thus enabling the possibility to describe the displacement field with second order polynomials.

Several mesh sizes have been used for the simulation, spanning from 0.25 mm to 2.5 mm. The results are benchmarked with the analytical curve, whose closed-form solution can be found in the Appendix D. The analytical expression which is used in this Figure belongs to a *Corrected Beam Theory* (CBT) approach, according to which the effective crack tip is considered to be larger than the pre-cracked region (Álvarez et al., 2014). It is important to recall that the CZL in this test was found to be 0.825 mm.

It is evident from Figure 5.20 that the threshold for this technology is 1 mm mesh size, that is, a mesh size to CZL ratio of 1.21. Compared to the results obtained from the other authors, this outcome is quite in line with the expectations, however, it must be considered that the CE is employing 30 IPs and reducing this number could negatively affect the result.

Since the employment of an adaptive integration scheme for the II Order CE would not have brought any further improvement on the accuracy of the solution, no implementation for adaptive integrations has been made. Therefore, no study has been made on the effectiveness of the solution in terms of computational time.

As previously reported in this report, the mode I opening is characterized by the most severe mesh constraint among the three opening modes. For this reason the DCB has been used as first benchmark to test the feasibility of the solution, and to quantify the improvements obtainable from the technology used. Therefore, testing the II Order CE under mixed mode and mode II has been believed to be superfluous.

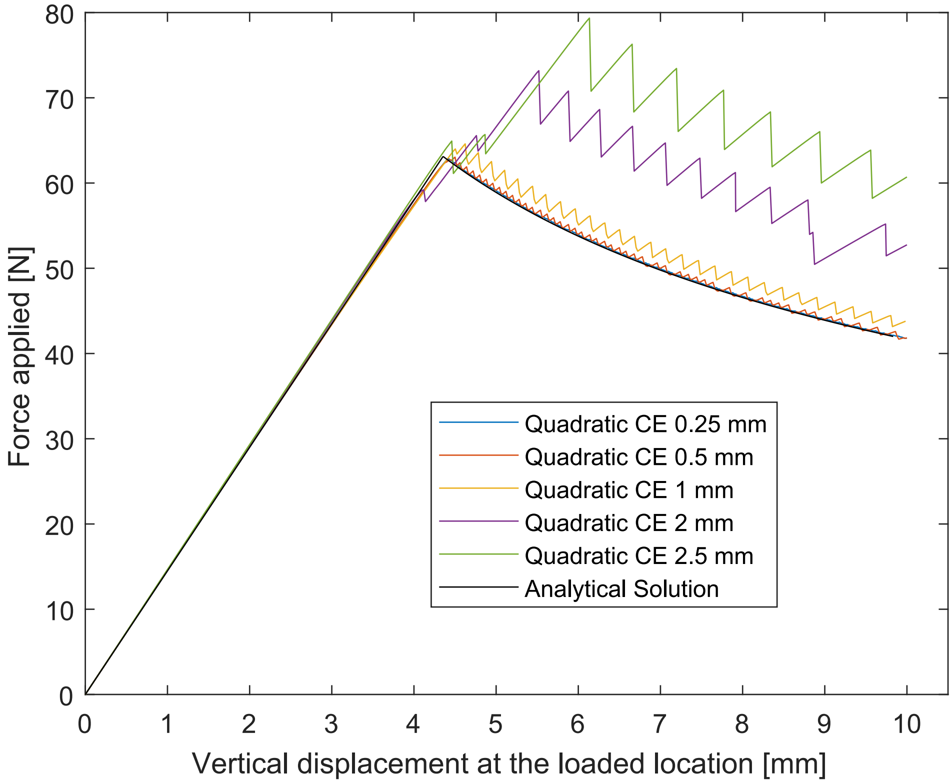

Figure 5.20: Load-Displacement results of the DCB test using II Order CEs with several mesh sizes.

5.5 III Order CEs DCB

The III order CE must be coupled with beam elements, therefore, Euler B23 elements have been used to model the substrates. The same properties used for the benchmark have been used to characterize the mechanical behavior of the beam elements. The generation of the input file of the analysis has been carried out in MATLAB®, so that the most important features, such as mesh size, could have been parametrized.

In Figure 5.21 the progress of the deformed shape of the specimen can be observed. In this figure, the configuration of the beam-elements model has been printed over the benchmark solution, so as to demonstrate that the global deformation of the structure is the same. This procedure has been done at different values of the opening. The black thick central line is the neutral axis of the beam elements, while the contoured elements on the background represent the benchmark.

The settings and the input file used for the simulation are collected in Appendix C. In Figure 5.22 the results of the implementation of the III Order CE can be observed in terms of load-displacement curves. The results are benchmarked with the analytical solution and the experimental results. The latter have not been produced by the author, but they have been taken from (Turon et al., 2006), where the same DCB case is physically tested. For comparison purposes, the curves belonging to the implementation of the linear CE with 0.25 mm and 2.5 mm mesh size are included.

The first information which could be extract from Figure 5.22 is the noteworthy improvement of the limitation in terms of mesh size. In fact, a substantial enlighten of the constrain on the mesh size took place. Using linear CEs would require a maximum element size of 0.25 mm in order to reach within 6.41% absolute average deviation from the experimental curve. With 2 mm and larger linear CEs, the results would be far off from the experimental ones. The predicted delamination initiation load was 185% of the experimental value with 2.5-mm linear CE, and this is now improved to 104% with the 2.5-mm proposed element. In the case of even larger CEs, no delamination is occurring within the time-step of the simulation, while the proposed 5-mm element's initiation strength prediction is at 108%. In terms of propagation, linear 2.5-mm CEs prediction is far off the experimental curve, whilst the proposed 2.5-mm and 5-mm elements predictions oscillate around the analytical curve.

(a) 4 mm normal opening.

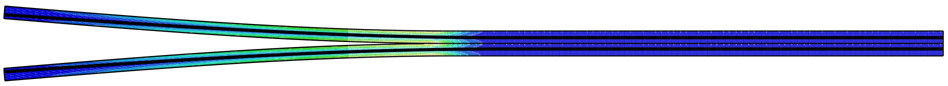

(b) 8 mm normal opening.

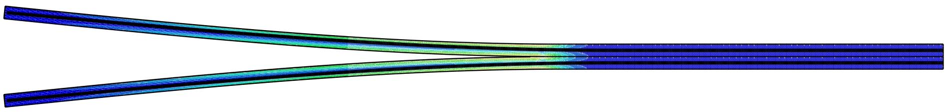

(c) 12 mm normal opening.

Figure 5.21: Comparison of deformed shape of the DCB specimen at different opening stages.

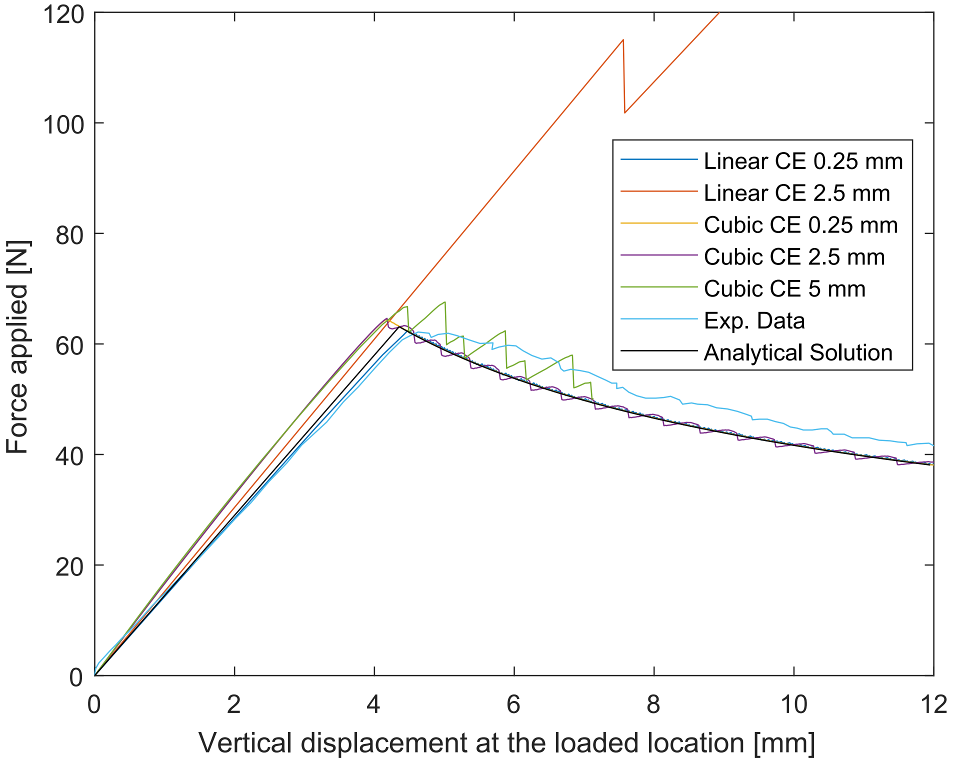

Figure 5.22: Load vs Displacement results of the DCB test obtained with different mesh sizes.

Another important difference which can be pointed, holds in the larger initial stiffness affecting the III order CE simulation. The reason of this gradually reducing difference in the initial stiffness has been attributed to the type of elements used to model the substrates. During the initial phase of the simulation, the CEs play a marginal role in the characterization of the response, and, at the same time, the behavior of the system is mainly driven by the reaction generated by the substrates. With an ever-increasing opening, the CEs provide an ever-increasing attractive force between the two substrates. Part of this stress is absorbed by the elements of the substrates, that, experiencing a traction force, slightly enlarge, therefore lightening the opening force that must be exerted at the vertex of the specimen to counteract the pulling force generated by the CEs. In case the elements used to model the substrates are not able to catch the same traction force, the whole pulling force generate by the CE falls completely at the opening vertexes of the specimen, meaning that a larger force is required at that location for a certain opening. The more the structural behavior is dominated by the response of the CEs, the more the mismatch between the stiffnesses decreases.

Figure D.2 depicts the analytical solution of the Corrected Beam Theory and the standard Euler Beam Theory. The CBT considers the pre-crack to be larger than its original value; the Euler beam theory does not account for the effect of the shear. In a physical test, the shear forces at the crack location are in the same order of magnitude of the normal forces (see Figure 5.5 and 5.6). Therefore, the CBT and the Euler theory represent two physical conditions, the first one more lenient and the second one stiffer. The fact that the curve generated by using III order CEs lies between these two solutions proves that the formulated hypotheses was correct.

	Linear 0.25 mm CEs	Cubic 2.5 mm CEs
# Elements	8901	158
# D.o.F.	11040	606
CPU Time	2606 s	47 s
Time/D.o.F.	0.236	0.077
# Iterations	7088	1123

Table 5.3: Performances of Linear and Cubic CEs in DCB test.

Many tests have been conducted, using Linear and III order CEs, and the most relevant be found in the Appendix B. However, to emphasize the gains in CPU time attained by using this method, a small comparison, including the key aspects of the trade-off, is reported in Table 5.5, between Linear and III order CEs performances.

Following the methodology used to quantify the improvements obtained by other authors, the largest CE mesh to CZL ratio achieved in the DCB simulation was 3, while a huge time saving was achieved (98%) but it is important to remember that modelling using the beam elements brings to a smaller number of degrees of freedom.

5.6 III Order CEs ENF

The input files of this test case have been generated using MATLAB®. Once again, in Figure 5.23, the deformed shapes obtained with Linear and III order CEs are overlapped such as to demonstrate that the same deformed geometries are obtained using solid or beam elements.

As it can be seen in Figure 5.23, the structure experiences a snapback, and it is also visible in Figure 5.24, where the results in terms of load-displacement for several mesh size are presented, benchmarked with the analytical solution and the results coming from the linear CEs.

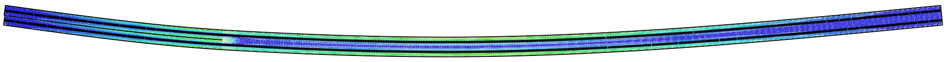

(a) 5 mm applied displacement.

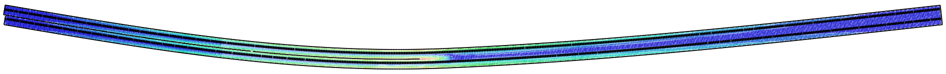

(b) 6.7 mm applied displacement.

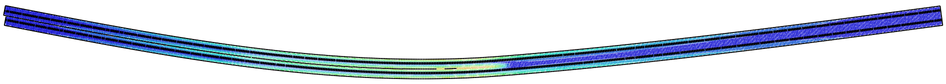

(c) 8.3 mm applied displacement.

Figure 5.23: Comparison of assumed shape of the DCB specimen during deformation at different opening stages.

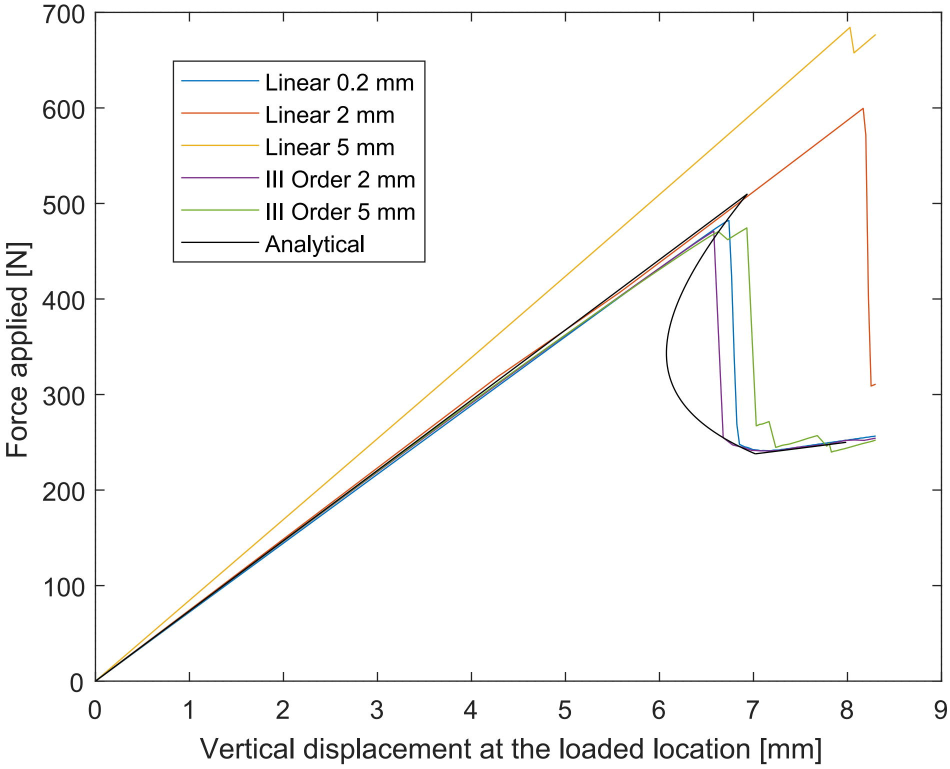

Figure 5.24: Load vs Displacement results of the DCB test obtained with different mesh sizes.

Capturing the snapback in a simulation is not always easy, and the fact that it was possible to overcome the instability and correctly predict the equilibrium configuration after the snapback using less equilibrium iteration is a sign of stability of the CE formulation. Diverse informations can be obtained from Figure 5.24.

The linear CEs would require a mesh size of 0.2 mm to obtain results in line with the analytical curve. Adopting 2 mm and 5 mm linear CE in this case would lead to an overshoot of the delamination onset by 115 % and 131% respectively. The curve belonging to the 5 mm linear CE size in Figure 5.24, besides capturing the delamination onset way off the analytical solution, it shows an overestimation of the initial stiffness. This is induced by the fact that ten elements through the thickness were used, thus resulting in a too slender element, which overestimates the bending stiffness of the arms. The 2 mm proposed CE provides an excel agreement with the analytical curve, although it must be noted that the model used to implement the novel element shows a slightly lower stiffness than the solid model. This induces the snapback to occur at 6.66 mm applied vertical displacement, while the same phenomena was predicted to happen at 6.83 mm in the benchmark. The 5 mm proposed element is able to predict the snapback within 3% deviance from the value of applied vertical displacement measured predicted in the benchmark.

As for the DCB case, in Table 5.6 the performances of the two types of CEs are reported, while the complete overview of the simulations are reported in appendix B.

	Linear 0.2 mm CEs	Cubic 2 mm CEs
# Elements	15925	208
# D.o.F.	33744	824
CPU Time	10552 s	47 s
Time/D.o.F.	0.312	0.057
# Iterations	9450	1123

Table 5.4: Performances of Linear and Cubic CEs in ENF test.

5.7 III Order CEs MMB

The last configuration tested, as said in Section 5.2, presented difficulties in converging to the analytical solution using Standard CEs. These same difficulties, however, were not encountered while using the III Order CEs/Beam elements, but this is not to be attributed to the CEs themselves, rather to the additional complexity in coupling the apparatus with the specimen. The main difference between the analytical curve and the Linear CEs solution is that the response of the Linear CE does not show any snapback, instead, a smooth transition is simulated. The results of the simulation can be observed in Figure 5.25.

The smooth transition simulated by the Standard CEs can be attributed, as previously stated, to the inability of the adopted set-up to ensure a 50% mixity mode throughout the fracture process zone, therefore inducing to a local damage history which totally differs form the one imposed by the user, corresponding to a 50% mixed mode opening. Nonetheless, both the user-defined elements, the one proposed here and the one by Turon et al. in (Turon et al., 2010), are able to predict the snapback.

Another element suggesting that the simulation is not completely correct is the difference in the deformed shapes assumed by the benchmark solution and the one proposed here.

For the MMB case, the same trend characterizing the previous study case have been confirmed: the employed High Order CE mesh size is one order of magnitude larger than the one used for the linear CEs.

	Linear 0.1 mm CEs	Cubic 2 mm CEs
# Elements	26490	144
# D.o.F.	55847	1092
CPU Time	32759 s	55 s
Time/D.o.F.	0.589	0.050
# Iterations	16619	1380

Table 5.5: Performances of Linear and Cubic CEs in MMB test.

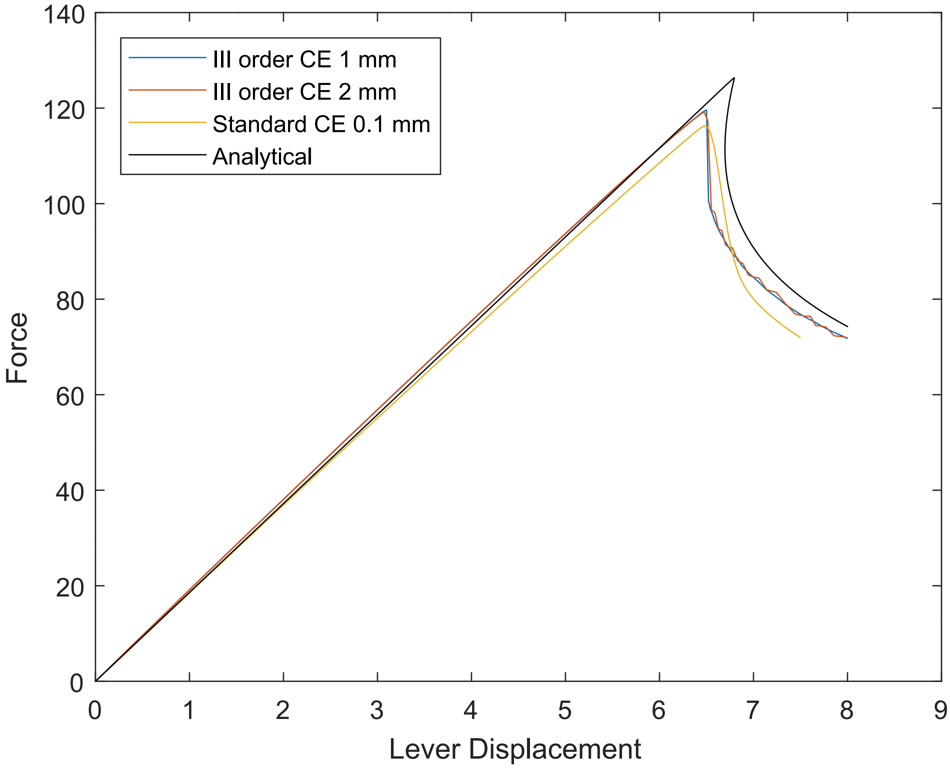

Figure 5.25: Load vs Displacement results of the MMB test obtained with different mesh sizes.

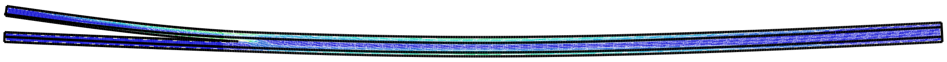

(a) 6 mm applied displacement on the lever.

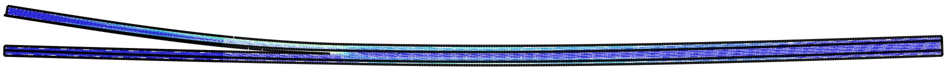

(b) 7 mm applied displacement on the lever.

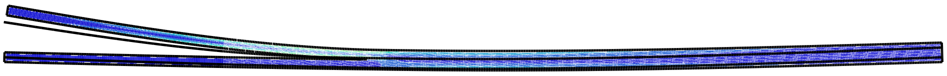

(c) 7.5 mm applied displacement on the lever.

Figure 5.26: Comparison of assumed shape of the MMB specimen during deformation at different opening stages.

Chapter 6

Conclusion and Recommendation

In this chapter, recalling the research object presented in the introduction of the report, the outcome of this study will be outlined, in parallel with the suggestions for future students taking over this line of research.

After a detailed review of the literature, the limit of applicability of the CZM technique for delamination purposes has been delineated in terms of mesh size compared to the length of the fracture process zone. Depending on the opening mode, the entity of the constraint varies, founding in the mode I opening the most compelling one. The root of the limitation lies in the strong gradient of the stress distribution around the crack tip, which needs to be properly captured. Researches have been conducted about possible solutions already proposed in literature, and inspiration has been taken from them. An analytical model of the CE has been developed and implemented in the solver ABAQUS, and a comparison has been made between the performance of the novel proposed method and the standard currently used technology.

From the comparison made in Chapter 5, it is evident that the high order adaptively integrated CE performs better than the standard linear CE. Due to the necessity of coupling this element with a high order element, the beam elements had to be used, therefore sensibly decreasing the time required to complete the simulation. However, when the comparison is made considering the CPU-time to degree-of-freedom ratio, the improvements are appreciable. The time required for the simulation to complete is, in general, two order of magnitude smaller than before, while retaining a response with the same degree of accuracy than the benchmarked one.

Furthermore, the high order CE demonstrated a much faster rate of convergence, measurable in terms of number of total iterations required to compete the analysis. This parameter is undoubtedly affected by the number of degree of freedom, but the closeness of the numerically-predicted response to the equilibrium configuration plays the major role in determining the number of total iterations required. As described in Section 4.1.2, the equilibrium configuration is found through an iterative process seeking for the zero of a function, and the stiffness is updated every iteration. When the CEs are implemented in a FE model, small incremental steps must be used, because the stiffness (degradation status) of a CE is highly sensible to changes of the opening. Therefore, especially when the crack propagates, the stiffness matrix of the whole system (being formed also by the combination of the stiffness matrices of the CEs) goes through severe changes. To better visualize the consequences, it is equivalent to consider a high nonlinear curve in Figure 4.4, where the steepness of the curve drastically changes between two consecutive iterations, leading to a larger number of iterations required. In this regard, the high order CE is able to perform a better evaluation of the residual forces and therefore a smoother convergence rate.

Another positive aspect which plays in favor of the implementation of the proposed solution is the fact that it has been tested in a relatively severe condition. The MMB and ENF case, are both affected by snapback, which is no trivial condition to simulated. The analytical curves showed in the Appendix D present a recess zone during crack propagation, and this instability cannot be captured with the solution technique used in this study, i.e. *Newton-Raphson* method. To step from an equilibrium configuration to next one, either an increment in the nodal forces or the nodal displacement is used as initial guess of the consecutive solution, but when a snap-back occurs, the system experience a discontinuous and abrupt drop of the stiffness, therefore requiring a negative increment of the force/displacement condition. The method to track this phenomenon is called *Riks method* or *Arc-Length method*, however, this different solution approach requires a different code that adapts to it, and this was not the scope of this research. Nonetheless, the fact that the high order CEs can simulate a sever condition as the one of the snap-back, is a proof of their robustness.

However, the advantages that this solution brings, are compensated by some other aspects that, for the sake of completeness, must be mentioned. The main limitation affecting this elements is related to the choice of the substrate elements. Because of compatibility and because of the proposed formulation, these CEs must be coupled with elements whose nodes have the rotational degree of freedom. Euler Beam elements have been therefore adopted within this research. The drawback of using beam elements is that no through-the-thickness phenomena can be captured.

Another limitations lies in the fact that adjacent elements share the information related to the rotation of the common node, implying that the displacement field is continuous in $\mathcal{C}^1$, that is, its derivative is continuous too, and in some cases, this could represent an over-constraint on the displacement field, especially when it is affected by steep variations.

Another negative aspect of the proposed technology is its partial incompatibility with multi-processing. In fact, it has been experienced that running the same analysis using more processors, would lead to not-convergence of the simulation, while using one or few processors leads to correct results. The aim of this research was not to deliver a ready-to-use tool for the software used (ABAQUS), such that it could be easily implemented, rather, the feasibility of the high order CEs had to be studied, therefore this downside is partially relevant. However, for future developments, the current incompatibility of the code with multi-threading deserved to be mentioned, also as possible future improvement of the code.

Regarding the future development of this line of research, the main recommendation would be to extent this technology to a 2D framework. This would represents the most important further development of the model, because it could be used to assess delamination on 2D composite structures modelled with shells, that are widely employed during the design stage instead of 1D structures as beam, used only as test case. This implies the adaptation of the code to a 2D domain, introducing also the second rotational degree of freedom, which should be properly handled. In the refined CEs 30 IP are used, however, for a 2D CE the suggestion would be to couple the High Order CE with a double Level Set description which helps identifying the area where the crack is propagating and therefore enrich that zone with a sub-domain integration scheme. Each one of the Level Set Description identifying an opening condition of the CEs, referring to crack onset (δ_0) and opened crack (δ_f).

To conclude, this research has investigated the feasibility of the adoption of High Order CEs to assess composite delamination in 1D. It has been established that, given the limitation of their implementation, High Order CEs can precisely predict the global behavior of a delaminating structure, gaining computational time while retaining the same degree of accuracy of the response compared to the current technology. However, further developments and tests are required to bring this technology accessible and employable for engineers, by enhancing the definition of CE into a 2D space.

References

01(2007)e2., A. D. . (2007), *Standard test method for mode I interlaminar fracture toughness of unidirectional fiber-reinforced polymer matrix composites*, ASTM Internat.

Alfano, G. and Crisfield, M. A. (2001), 'Finite element interface models for the delamination analysis of laminated composites: Mechanical and computational issues', *International Journal for Numerical Methods in Engineering* **50**(7), 1701–1736.

Álvarez, D., Blackman, B. R. K., Guild, F. J. and Kinloch, A. J. (2014), 'Mode I fracture in adhesively-bonded joints: A mesh-size independent modelling approach using cohesive elements', *Engineering Fracture Mechanics* **115**, 73–95.

Barenblatt, G. (1962), The Mathematical Theory of Equilibrium Cracks in Brittle Fracture, *in* 'Advances in Applied Mechanics', Elsevier, pp. 55–129.

Bazant, Z. P. and Planas, J. (1997), *Fracture and size effect in concrete and other quasibrittle materials*, Vol. 16, CRC press.

Benzeggagh, M. and Kenane, M. (1996), 'Measurement of mixed-mode delamination fracture toughness of unidirectional glass/epoxy composites with mixed-mode bending apparatus', *Composites Science and Technology* **56**(4), 439–449.

Bezant, P. and Planas, J. (1998), *Fracture and size effect in concrete and other quasi brittle materials*, CRC Press.

Camanho, P. and Davila, C. (2002), 'Numerical Simulation of Mixed-mode Progressive Delamination in Composite Materials', *Nasa* **TM-2002-21**(June), 1–37.

Chen, B., Tay, T., Pinho, S. and Tan, V. (2016), 'Modelling the tensile failure of composites with the floating node method', *Computer Methods in Applied Mechanics and Engineering* **308**, 414–442.

Chen, B. Y., Pinho, S. T., De Carvalho, N. V., Baiz, P. M. and Tay, T. E. (2014), 'A floating node method for the modelling of discontinuities in composites', *Engineering Fracture Mechanics* **127**, 104–134.

Corigliano, A. (1993), ‘Formulation, identification and use of interface models in the numerical analysis of composite delamination’, *International Journal of Solids and Structures* **30**(20), 2779–2811.

Cox, B. and Marshall, D. (1994), ‘Concepts for bridged cracks in fracture and fatigue’, *Acta Metallurgica et Materialia* **42**(2), 341–363.

Cui, W. and Wisnom, M. (1993), ‘A combined stress-based and fracture-mechanics-based model for predicting delamination in composites’, *Composites* **24**(6), 467–474.

Do, B. C., Liu, W., Yang, Q. D. and Su, X. Y. (2013), ‘Improved cohesive stress integration schemes for cohesive zone elements’, *Engineering Fracture Mechanics* **107**, 14–28.

Dudgale, D. (1960), ‘Yielding of steel sheets containing slits’, *Journal of the Mechanics and Physics of Solids* **8**(2), 100–104.

Falk, M. L., Needleman, A. and Rice, J. R. (2001), ‘A critical evaluation of cohesive zone models of dynamic fractur’, *Le Journal de Physique IV* **11**(PR5), Pr5–43.

Griffith, A. A. (1921), ‘The Phenomena of Rupture and Flow in Solids’, *Philosophical Transactions of the Royal Society A: Mathematical, Physical and Engineering Sciences* **221**(582-593), 163–198.

Guiamatsia, I., Ankersen, J. K., Davies, G. A. O. and Iannucci, L. (2009), ‘Decohesion finite element with enriched basis functions for delamination’, *Composites Science and Technology* **69**(15-16), 2616–2624.

Guiamatsia, I., Davies, G. A. O., Ankersen, J. K. and Iannucci, L. (2010), ‘A framework for cohesive element enrichment’, *Composite Structures* **92**(2), 454–459.

Harper, P. W. and Hallett, S. R. (2008), ‘Cohesive zone length in numerical simulations of composite delamination’, *Engineering Fracture Mechanics* **75**(16), 4774–4792.

Harper, P. W., Sun, L. and Hallett, S. R. (2012), ‘A study on the influence of cohesive zone interface element strength parameters on mixed mode behaviour’, *Composites Part A: Applied Science and Manufacturing* **43**(4), 722–734.

Hildebrand, F. B. (1987), *Introduction to numerical analysis*.

Hillerborg, A., Modéer, M. and Petersson, P. E. (1976), ‘Analysis of crack formation and crack growth in concrete by means of fracture mechanics and finite elements’, *Cement and Concrete Research* **6**(6), 773–781.

Hui, C.-Y., Jagota, A., Bennison, S. and Londono, J. (2003), Crack blunting and the strength of soft elastic solids, *in* ‘Proceedings of the Royal Society of London A: Mathematical, Physical and Engineering Sciences’, Vol. 459, The Royal Society, pp. 1489–1516.

Irwin, G. (1997), ‘Plastic zone near a crack and fracture toughness’.

Irwin, G. R. (1957), ‘Analysis of stresses and strains near the end of a crack traversing a plate’, *Journal of Applied Mechanic* .

Krueger, R. (2015), ‘A summary of benchmark examples to assess the performance of quasi-static delamination propagation prediction capabilities in finite element codes’, *Journal of Composite Materials* **49**(26), 3297–3316.

Li, B., Li, Y. and Su, J. (2014), ‘A combined interface element to simulate interfacial fracture of laminated shell structures’, *Composites Part B: Engineering* **58**, 217–227.

Ling, D., Yang, Q. and Cox, B. (2009), ‘An augmented finite element method for modeling arbitrary discontinuities in composite materials’, *International Journal of Fracture* **156**(1), 53–73.

Lu, X., Chen, B., Tan, V. and Tay, T. (2018), ‘Adaptive floating node method for modelling cohesive fracture of composite materials’, *Engineering Fracture Mechanics* **194**(March), 240–261.

Massabo, R. and Cox, B. N. (1999), ‘Concepts for bridged Mode II delamination cracks’, *Journal of the Mechanics and Physics of Solids* **47**(6), 1265–1300.

Mi, Y., Crisfield, M. A., Davies, G. A. O. and Hellweg, H. B. (1998), ‘Progressive Delamination Using Interface Elements’, *Journal of Composite Materials* **32**(14), 1246–1272.

Moës, N. and Belytschko, T. (2002), ‘Extended finite element method for cohesive crack growth’, *Engineering Fracture Mechanics* **69**(7), 813–833.

Needleman, A. (1987), ‘A Continuum Model for Void Nucleation by Inclusion Debonding’, *Journal of Applied Mechanics* **54**(3), 525.

Pirondi, A., Giuliese, G., Moroni, F., Bernasconi, A. and Jamil, A. (2014), ‘Comparative Study of Cohesive Zone and Virtual Crack Closure Techniques for Three-Dimensional Fatigue Debonding’, *The Journal of Adhesion* **90**(5-6), 457–481.

Rice, J. (1979), *The mechanics of earthquake rupture*, Division of Engineering, Brown University.

Rybicki, E. F. and Kanninen, M. F. (1977), ‘A finite element calculation of stress intensity factors by a modified crack closure integral’, *Engineering Fracture Mechanics* **9**(4), 931–938.

Samimi, M., van Dommelen, J. A. W. and Geers, M. G. D. (2009), ‘An enriched cohesive zone model for delamination in brittle interfaces’, *International Journal for Numerical Methods in Engineering* **80**(5), 609–630.

Samimi, M., Van Dommelen, J. A. W. and Geers, M. G. D. (2011), ‘A self-adaptive finite element approach for simulation of mixed-mode delamination using cohesive zone models’, *Engineering Fracture Mechanics* **78**(10), 2202–2219.

Shet, C. and Chandra, N. (2004), ‘Effect of the Shape of T âĂŞδ Cohesive Zone Curves on the Fracture Response’, *Mechanics of Advanced Materials and Structures* **11**(3), 249–275.

Smith, E. (1989), ‘The failure of a strain-softening material: I. Analytical approach for a double cantilever beam specimen’, *Theoretical and Applied Fracture Mechanics* **11**(1), 59–64.

Song, J. H., Areias, P. M. A. and Belytschko, T. (2006), ‘A method for dynamic crack and shear band propagation with phantom nodes’, *International Journal for Numerical Methods in Engineering* **67**(6), 868–893.

Soto, A., González, E., Maimí, P., Turon, A., Sainz de Aja, J. and de la Escalera, F. (2016), ‘Cohesive zone length of orthotropic materials undergoing delamination’, *Engineering Fracture Mechanics* **159**, 174–188.

Standard, A. (2006), ‘D6671/d6671m (2006) standard test method for mixed mode i-mode ii interlaminar fracture toughness of unidirectional fiber reinforced polymer matrix composites’, *ASTM International, West Conshohocken, PA. doi* **10**, D6671_D6671M.

Turon, A., Camanho, P., Costa, J. and Dávila, C. (2006), ‘A damage model for the simulation of delamination in advanced composites under variable-mode loading’, *Mechanics of Materials* **38**(11), 1072–1089.

Turon, A., Camanho, P. P., Costa, J. and Renart, J. (2010), ‘Accurate simulation of delamination growth under mixed-mode loading using cohesive elements: Definition of interlaminar strengths and elastic stiffness’, *Composite Structures* **92**(8), 1857–1864.

Turon, A., Costa, J., Camanho, P. P. and Maimí, P. (2008), ‘Analytical and Numerical Investigation of the Length of the Cohesive Zone in Delaminated Composite Materials’, *Mechanical Response of Composites* **10**, 77–97.

Turon, A., Dávila, C. G., Camanho, P. P. and Costa, J. (2007), ‘An engineering solution for mesh size effects in the simulation of delamination using cohesive zone models’, *Engineering Fracture Mechanics* **74**(10), 1665–1682.

Tvergaard, V. and Hutchinson, J. W. (1992), ‘The relation between crack growth resistance and fracture process parameters in elastic-plastic solids’, *Journal of the Mechanics and Physics of Solids* **40**(6), 1377–1397.

Yang, Q. and Cox, B. (2005), ‘Cohesive models for damage evolution in laminated composites’, *International Journal of Fracture* **133**(2), 107–137.

Yang, Q. D., Fang, X. J., Shi, J. X. and Lua, J. (2010), ‘An improved cohesive element for shell delamination analyses’, *International Journal for Numerical Methods in Engineering* .

Appendix A

Appendix A: Derivative of the Φ matrix

Due to simplify the equations, the matrix $\mathbf{\Phi}$ has been dived in its first and second row; the first one, multiplied by $\boldsymbol{\delta}_L$ returns the mode I opening, while if the second row was used, the mode II opening is obtained. From Equation 4.15, the nabla operator, meant to be a column vector, is multiplying the first raw of the $\mathbf{\Phi}$ matrix. From equation 4.7, the resulting matrix has the following form:

$$\begin{bmatrix} \frac{\partial \cos(\alpha_\Gamma)}{\partial u_1} & \frac{\partial \sin(\alpha_\Gamma)}{\partial u_1} \\ \frac{\partial \cos(\alpha_\Gamma)}{\partial u_2} & \frac{\partial \sin(\alpha_\Gamma)}{\partial u_2} \\ \frac{\partial \cos(\alpha_\Gamma)}{\partial u_3} & \frac{\partial \sin(\alpha_\Gamma)}{\partial u_3} \\ \vdots & \vdots \\ \frac{\partial \cos(\alpha_\Gamma)}{\partial u_{12}} & \frac{\partial \sin(\alpha_\Gamma)}{\partial u_{12}} \end{bmatrix} \tag{A.1}$$

Due to the fact that the components of $\mathbf{\Phi}_{II}$ are the same as $\mathbf{\Phi}_I$, only differently arranged, the results coming from the latter can be used to fill in the former. Each partial derivative has been carried out using the software Wolfram Mathematica®, and the code is here reported for II and III Order CEs respectively:

```

(*Computing the derivatives of the components of the PHI matrix for the ...
    III Order CE*)

vCETp[N1p_,N2p_,N3p_,u12_,u10_,u8_]:=N1p*u12+N2p*u10+N3p*u8

vCEBp[N1p_,N2p_,N3p_,u2_,u4_,u6_]:=N1p*u2+N2p*u4+N3p*u6

```

```
hCETp[N1p_,N2p_,N3p_,u11_,u9_,u7_]:=N1p*u11+N2p*u9+N3p*u7

hCEBp[N1p_,N2p_,N3p_,u1_,u3_,u5_]:=N1p*u1+N2p*u3+N3p*u5

alpha[N1p_,N2p_,N3p_,u12_,u10_,u8_,u2_,u4_,u6_,u1_,u3_,u5_,u11_,
 u9_,u7_,u12_,u10_,u8_,L_]:=
 ArcTan[(vCETp[N1p,N2p,N3p,u12,u10,u8]+vCEBp[N1p,N2p,N3p,u2,u4,u6])/
 (L+hCETp[N1p,N2p,N3p,u11,u9,u7]+hCEBp[N1p,N2p,N3p,u1,u3,u5])]

f[N1p_,N2p_,N3p_,u12_,u10_,u8_,u2_,u4_,u6_,u1_,u3_,u5_,u11_,u9_,
 u7_,u12_,u10_,u8_,L_]:=
 Cos[alpha[N1p,N2p,N3p,u12,u10,u8,u2,u4,u6,u1,u3,u5,u11,u9,u7,u12,u10,u8,L]]

g[N1p_,N2p_,N3p_,u12_,u10_,u8_,u2_,u4_,u6_,u1_,u3_,u5_,u11_,u9_,
 u7_,u12_,u10_,u8_,L_]:=
 Sin[alpha[N1p,N2p,N3p,u12,u10,u8,u2,u4,u6,u1,u3,u5,u11,u9,u7,u12,u10,u8,L]]
```

```

(*Computing the derivatives of the components of the PHI matrix for the ...
    III Order CE*)

thetaBB[Nt1_,Nt2_,Nt3_,Nt4_,u2_,u3_,u5_,u6_]:=Nt1*u2+Nt2*u3+Nt3*u5+Nt4*u6

thetaBT[Nt1_,Nt2_,Nt3_,Nt4_,u11_,u12_,u8_,u9_]:=Nt1*u11+Nt2*u12+Nt3*u8+Nt4*u9

vCET[Nt1_,Nt2_,Nt3_,Nt4_,Nv1_,Nv2_,Nv3_,Nv4_,u11_,u12_,u8_,u9_,h_] := ...
    Nv1*u11+Nv2*u12+Nv3*u8+Nv4*u9 + ...
    (h/2)*(1-Cos[thetaBT[Nt1,Nt2,Nt3,Nt4,u11,u12,u8,u9]])

vCEB[Nt1_,Nt2_,Nt3_,Nt4_,Nv1_,Nv2_,Nv3_,Nv4_,u2_,u3_,u5_,u6_,h_] := Nv1 ...
    u2+Nv2 u3+Nv3 u5+Nv4 u6+1/2 h (Cos[thetaBB[Nt1,Nt2,Nt3,Nt4,u2,u3,u5,u6]]-1)

hCET[Nh1_,Nh2_,Nt1_,Nt2_,Nt3_,Nt4_,u10_,u7_,u11_,u12_,u8_,u9_,h_] := Nh1 ...
    u10 + Nh2 u7 + (h/2) * Sin[thetaBT[Nt1,Nt2,Nt3,Nt4,u11,u12,u8,u9]]

hCEB[Nh1_,Nh2_,Nt1_,Nt2_,Nt3_,Nt4_,u1_,u4_,u2_,u3_,u5_,u6_,h_] := Nh1 u1 + ...
    Nh2 u4 + (h/2) * Sin[thetaBB[Nt1,Nt2,Nt3,Nt4,u2,u3,u5,u6]]

vCET[Nt1,Nt2,Nt3,Nt4,Nv1,Nv2,Nv3,Nv4,u11,u12,u8,u9,h]- ...
    vCEB[Nt1,Nt2,Nt3,Nt4,Nv1,Nv2,Nv3,Nv4,u2,u3,u5,u6,h]

hCET[Nh1,Nh2,Nt1,Nt2,Nt3,Nt4,u10,u7,u11,u12,u8,u9,h] - ...
    hCEB[Nh1,Nh2,Nt1,Nt2,Nt3,Nt4,u1,u4,u2,u3,u5,u6,h]

thetaBTp[Nt1p_,Nt2p_,Nt3p_,Nt4p_,u11_,u12_,u8_,u9_] := Nt1p u11 + Nt2p u12 ...
    + Nt3p u8 + Nt4p u9

vCETp[Nv1p_,Nv2p_,Nv3p_,Nv4p_,Nv1_,Nv2_,Nv3_,Nv4_,Nt1_,Nt2_,Nt3_,Nt4_,Nt1p_, ...
    Nt2p_,Nt3p_,Nt4p_,u11_,u12_,u8_,u9_,h_] :=
Nv1p u11 + Nv2p u12 + Nv3p u8 + Nv4p u9 +(h/2) * ...
    (Sin[thetaBT[Nt1,Nt2,Nt3,Nt4,u11,u12,u8,u9]]) * ...
    thetaBTp[Nt1p,Nt2p,Nt3p,Nt4p,u11,u12,u8,u9]

thetaBBp[Nt1p_,Nt2p_,Nt3p_,Nt4p_,u2_,u3_,u5_,u6_]:=Nt1p u2 + Nt2p u3 + ...
    Nt3p u5 + Nt4p u6

```

```
vCEBp[Nv1p_,Nv2p_,Nv3p_,Nv4p_,Nv1_,Nv2_,Nv3_,Nv4_,Nt1_,Nt2_,Nt3_,Nt4_, ...
    Nt1p_,Nt2p_,Nt3p_,Nt4p_,u2_,u3_,u5_,u6_,h_] :=
Nv1p u2 + Nv2p u3 + Nv3p u5 + Nv4p u6 -(h/2) * ...
    (Sin[thetaBB[Nt1,Nt2,Nt3,Nt4,u2,u3,u5,u6]]) * ...
    thetaBBp[Nt1p,Nt2p,Nt3p,Nt4p,u2,u3,u5,u6]

hCETp[Nt1p_,Nt2p_,Nt3p_,Nt4p_,Nh1_,Nh2_,Nt1_,Nt2_,Nt3_,Nt4_,u10_,u7_,u11_, ...
    u12_,u8_,u9_,h_] :=
(1/2) * (-u10+u7+h*Cos[thetaBT[Nt1,Nt2,Nt3,Nt4,u11,u12,u8,u9]] * ...
    thetaBTp[Nt1p,Nt2p,Nt3p,Nt4p,u11,u12,u8,u9])

hCEBp[Nt1p_,Nt2p_,Nt3p_,Nt4p_,Nh1_,Nh2_,Nt1_,Nt2_,Nt3_,Nt4_,u1_,u4_,u2_ ...
    ,u3_,u5_,u6_,h_] :=
(1/2) * (-u1+u4-h*Cos[thetaBB[Nt1,Nt2,Nt3,Nt4,u2,u3,u5,u6]] * ...
    thetaBBp[Nt1p,Nt2p,Nt3p,Nt4p,u2,u3,u5,u6])

alpha[Nh1_,Nh2_,Nv1p_,Nv2p_,Nv3p_,Nv4p_,Nv1_,Nv2_,Nv3_,Nv4_, ...
    Nt1p_,Nt2p_,Nt3p_,Nt4p_,Nt1_,Nt2_,Nt3_,Nt4_,u1_,u2_,u3_,u4_,u5_,u6_,u7_,u8_,u9_, ...
    u10_,u11_,u12_,h_,L_] :=
ArcTan[(vCETp[Nv1p,Nv2p,Nv3p,Nv4p,Nv1,Nv2,Nv3,Nv4,Nt1,Nt2 ...
    ,Nt3,Nt4,Nt1p,Nt2p,Nt3p,Nt4p,u11,u12,u8,u9,h] + ...
    vCEBp[Nv1p,Nv2p,Nv3p,Nv4p,Nv1,Nv2,Nv3,Nv4,Nt1,Nt2,Nt3,Nt4,Nt1p, ...
    Nt2p,Nt3p,Nt4p,u2,u3,u5,u6,h])/
(L+hCEBp[Nt1p,Nt2p,Nt3p,Nt4p,Nh1,Nh2,Nt1,Nt2,Nt3,Nt4,u1,u4,u2,u3,u5,u6,h] ...
    + ...
    hCETp[Nt1p,Nt2p,Nt3p,Nt4p,Nh1,Nh2,Nt1,Nt2,Nt3,Nt4,u10,u7,u11,u12,u8,u9,h])]

f[Nh1_,Nh2_,Nv1p_,Nv2p_,Nv3p_,Nv4p_,Nv1_,Nv2_,Nv3_,Nv4_,Nt1p_, ...
    Nt2p_,Nt3p_,Nt4p_,Nt1_,Nt2_,Nt3_,Nt4_,u1_,u2_,u3_,u4_,u5_,u6_, ...
    u7_,u8_,u9_,u10_,u11_, u12_,h_,L_] := ...
    Cos[alpha[Nh1,Nh2,Nv1p,Nv2p,Nv3p,Nv4p, ...
    Nv1,Nv2,Nv3,Nv4,Nt1p,Nt2p,Nt3p,Nt4p,Nt1,Nt2,Nt3,Nt4,u1,u2, ...
    u3,u4,u5,u6,u7,u8,u9,u10,u11,u12,h,L]]

g[Nh1_,Nh2_,Nv1p_,Nv2p_,Nv3p_,Nv4p_,Nv1_,Nv2_,Nv3_,Nv4_,Nt1p_, ...
    Nt2p_,Nt3p_,Nt4p_,Nt1_,Nt2_,Nt3_,Nt4_,u1_,u2_,u3_,u4_,u5_,u6_, ...
    u7_,u8_,u9_,u10_,u11_, u12_,h_,L_] := ...
    Sin[alpha[Nh1,Nh2,Nv1p,Nv2p,Nv3p,Nv4p, ...
    Nv1,Nv2,Nv3,Nv4,Nt1p,Nt2p,Nt3p,Nt4p,Nt1,Nt2,Nt3,Nt4,u1,u2, ...
    u3,u4,u5,u6,u7,u8,u9,u10,u11,u12,h,L]]
```

The derivatives of the functions f and g are then evaluated with respect to the variable u_1, u_2, u_3, ..., u_{12} and inputted in the main code.

Appendix B

Appendix B: Abscissas and weight of the Integration Points

The locations and the weights to be attiributed to the IPs have been estimated by determining the roots of the Legendre polynomial for n = 30:

$$P_n(x) = \frac{1}{2\pi i} \oint \left(1 - 2tx + r^2\right)^{\frac{1}{2}} t^{-n-1} dt \tag{B.1}$$

While the weights have been computed from teh following equation:

$$w_i = -\frac{2}{\left(1 - x_i^2\right)\left[P_n(x_i)'\right]^2} \tag{B.2}$$

The rigorous procedure can be found in (Hildebrand, 1987). The roots have been found adopting the software Wolfram Mathematica®, and the code is here presented:

```
symboliclegendre[n_,x_]:=Solve[LegendreP[n,x]==0];
legendreprime[n_,a_]:=D[LegendreP[n,x],x]/.x->a;
weights[n_,x_]:=2/((1-x^2) legendreprime[n,x]^2);

(*how many terms should be generated*)
h=30;

(*what numerical precision is desired?*)
precision=288;

str=OpenWrite[FileNameJoin[{NotebookDirectory[],"abscissae.txt"}]];
Write[str];
Do[Write[str];Write[str,n];Write[str];
  nlist=symboliclegendre[n,x];
  xnlist=x/.nlist;
```

```
  Do[Write[str,FortranForm[N[Part[xnlist,i],precision]]],
   {i,Length[xnlist]}];,{n,30,h}];
Close[str];
str=OpenWrite[FileNameJoin[{NotebookDirectory[],"weights.txt"}]];
Write[str];
Do[Write[str];Write[str,n];Write[str];
  slist:=symboliclegendre[n,x];
  xslist=x/.slist;
  Do[Write[str,FortranForm[N[weights[n,Part[xslist,i]],precision]]],
   {i,Length[xslist]}];,{n,30,h}];
Close[str];
```

The values of the weights and the abscissas are not reported here, to avoid overwriting.

Appendix C

Appendix C: Conducted Tests

In this appendix, further details regarding the numerical simulations are presented. Every test has been performed using different settings for the increments and the solution control parameters. The latter are rarely tuned for the specific simulated case, however, since CEs bring a large non-linearity in the system, properly modify them is a necessary requirement to ensure convergence. However, the choices of these parameters influence not only the success of the simulation but also the time required to achieve it. Therefore, to better evaluate the capabilities of the new CE, they are reported here. Two numbers have been used in the step/control setting cells, suggesting that the simulations has been divided in two steps.

For the MMB and ENF case, the excessive number of iterations required to converge are motivated by the presence of the snapback. In the ENF case, an additional simulation has been done using the contact condition between the two pre-cracked substrates, resulting in additional time saving.

The light red cells indicate the simulations that have been used to make the comparison in the Chapter 5.

Not all the simulations have been performed using the adaptively integrated CE, and, for this reason, the distinction is delineated in the following tables.

	# CEs	# DOF	CONTROL SET	STEP SET	# ITERATIONS	CPU TIME [#CPUs]
LINEAR	760 (0,125 mm)	19584	1	2	6244	3884 s [4]
	380 (0,25 mm)	11040	1	2	7088	2606 s [4]
	38 (2,5 mm)	1608	2	3	716	94 s [4]
III ORDER 30 IP	380 (0,25 mm)	4356	1	2	2166	657 s [4]
	380 (0,25 mm)	4356	1	1	909	220 s [4]
	38 (2,5 mm)	606	1	1	1123	54 s [4]
III ORDER ADAPTIVE	380 (0,25 mm)	4356	1	2	2178	562 s [4]
	38 (2,5 mm)	606	1	2	3511	176 s [4]
	38 (2,5 mm)	606	1	1	1123	47 s [4]

Table C.1: Summary of the DCB tests conducted.

CONTROL SETTING

	I0	Ir	Ip	Ic	Il	Ig	Is	Ia
1	200	400	10	450	500	10	//	10
2	800	1000	//	1500	1200	50	//	125

STEP SETTING

	nlGeom	Initial Increment	Total Time Step	Minimum Increment	Maximum Increment	Algorithm	BC
1	YES	0,01	1	1,00E-10	0,01 (0,06 mm)	Quasi-Newton	6 (velocity)
2	YES	0,01	6	1,00E-10	0,01 (0.01 mm)	Quasi-Newton	1(velocity)
3	NO	0,01	6	1,00E-10	0,01 (0.01 mm)	Quasi-Newton	1(velocity)

Table C.2: Step Setting and Controls used for the DCB tests.

	# CEs	# DOF	CONTROL SET	STEP SET	# ITERATIONS	CPU TIME [# CPU]
LINEAR	115(1mm)	6784	1 1	1 2	18889	5908 s [4]
	58(2mm)	3460	1 1	1 2	3867	769 s[4]
	23(5mm)	1392	1 1	1 2	2704	246 s[4]
	575(0,2mm)	33744	1 1	6 7	9450	10552 s[4]
	329(0,35mm)	19320	1	8	11349	7359 s[4]
	231(0,5mm)	13524	1	8	12215	5687 s[4]
	575(0,2mm)	33744	5	5	829	994 s[4]
III ORDER	1500 (0,1mm)	15006	2 3	3 4	1852	2860 s [16]
	75(2 mm)	756	2 3	3 4	2405	522 s [20]
	75(2 mm)	756	5	5	1485	89 s [4]
	30(5mm)	306	2 3	3 4	4231	655 s [20]
	30(5mm)	306	2 3	3 4	3238	237 s [4]
	30(5mm)	306	2	5	1048	41 s [4]
III ORDER ADAPTIVE	75(2 mm)	756	5	5	1650	92 s [4]
III ORDER ADAPTIVELY + CONTACT	58(2mm)	824	5	5	930	47 s [4]

Table C.3: Summary of the ENF tests conducted.

	CONTROL SETTING							
	I0	Ir	Ip	Ic	Il	Ig	Is	Ia
1	800	1000	900	1600	1000	400	1200	500
2	100	200	500	300,00	500	20	//	10
3	1000	1250	1100	1300,00	1000	20	//	10
4	200	400	10	450,00	500	10	//	10
5	20	80	300	300,00	310	10	//	10

	STEP SETTING							
	nlGeom	Extrapolation	Initial Increment	Total Time Step	Minimum Increment	Maximum Increment	Algorithm	BC
1	YES	NO	0,01	1	1,0E-20	0,01	Newton	5,5 mm
2	YES	NO	1,00E-08	1,00	1,0E-20	0,001	Newton	8,3 mm
3	NO	Linear	1,00E-09	6,30	1,00E-20	0,01	Newton	1 (velocity)
4	NO	Linear	0,001	2,00	1,00E-20	0,01	Quasi-Newton	1 (velocity)
5	NO	Linear	0,001	8,30	1,00E-20	0,1	Quasi-Newton	1(velocity)
6	NO	Linear	0,01	1	1,0E-20	0,01	Newton	5,5 mm
7	NO	Linear	1,00E-08	1,00	1,0E-20	0,001	Newton	8,3 mm
8	NO	Linear	1,00E-09	8,30	1,00E-20	0,01	Newton	1(velocity)

Table C.4: Step Setting and Controls used for the ENF tests.

	# CEs	# DOF	CONTROL SET	STEP SET	# ITERATIONS	CPU TIME [# CPUs]
LINEAR	1150	55847	2 2	3 4	16619	32759 s [3]
III ORDER 30 IP	1150(0.1mm)	12012	1 2	1 2	1638	2180 s [20]
	22 (5 mm)	742	1	5	887	242 s [1]
III ORDER ADAPTIVE	1150(0.1mm)	12012	1 2	1 2	1634	464 s [1]
	575(0.2mm)	6262	1	5	3517	512 s [1]
	329 (0.35mm)	3802	2	5	1273	112 s [1]
	230 (0.5mm)	2812	2	5	1420	97 s [1]
	115 (1mm)	1662	1	5	1680	87 s [1]
	58 (2mm)	1092	1	5	1380	55 s [1]

Table C.5: Summary of the MMB tests conducted.

CONTROL SETTING

	I0	Ir	Ip	Ic	Il	Ig	Is	Ia
1	100	200	500	300	500	20	//	10
2	800	1000	900	1600,00	1000	400	//	15

STEP SETTING

	nlGeom	Extrapolation	Initial Increment	Total Time Step	Minimum Increment	Maximum Increment	Algorithm	BC
1	NO	Linear	0,01	6	1,0E-10	0,1	Quasi-Newton	-1 (velocity)
2	NO	Linear	0,01	1,70	1,0E-10	0,01	Quasi-Newton	-1 (velocity)
3	YES	Linear	0,01	1,00	1,0E-20	0,01	Newton	-5 mm
4	YES	NO	1,00E-08	1,00	1,0E-20	0,001	Newton	-7,5 mm
5	NO	Linear	0,01	8	1,0E-10	0,1	Quasi-Newton	-1 (velocity)

Table C.6: Step Setting and Controls used for the MMB tests.

Appendix D

Appendix D: Closed-Form solutions of the DCB, MMB and ENF load displacement relationships.

The closed form solutions of the load displacement laws are taken from (Turon et al., 2010), where the author retrieves the ASTM standards for DCB, MMB and ENF tests (01, 2007; Standard, 2006). However, for the DCB case, another formulations is used, derived under the assumption of the *Corrected Beam Theory* (CBT). This theory accounts for the fact that the fracture process zone degrades before the crack onset occurs, due to stress concentration. The pre-degradation of the cohesive zone induces the structure to experience a larger initial crack, effectively equal to the pre-cracked length, plus an additional contribute, which depends on the material properties and the thickness of the composite laminate (Harper and Hallett, 2008). It must be noted that the equations reported by Turon for MMB already accounts for CBT.

Referring to Figure D.1, three discontinuous curves might be recognized, A, B and C, described by three different equations and describing three different phenomena. Curve A belongs to the linear trait, the crack has not propagated yet, and the structure reacts with a linear response. In this part either the Euler Beam or the Corrected Beam Theories can be used. The curve B describes the response of the structures when the crack is stationary growing, under the hypothesis that the crack is extended for less than half the length of the specimen. In case the crack propagates further, the equations belonging to the trait C have to be used. The equations of the C curve for the ENF tests can be found in (Mi et al., 1998). This condition verifies only in the case of the ENF test, therefore the C part of the curve can be observed only in that case.

For the DCB, ENF and MMB tests the graphs have the same form, the main difference lies in the description of the trait B, where a snapback might occur, because instable crack growth affects the specimen, meaning that the trait B will present a more pronounced recess.

The equations are the following:

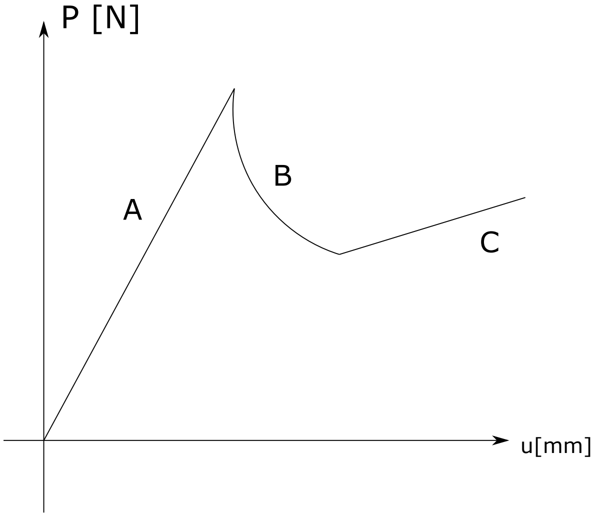

Figure D.1: General shape of the Load-displacement graph for the DCB, MMB and ENF test.

$$DCB\begin{cases} A \implies u = \dfrac{2P(a_0+\chi t)^3}{3E_{11}I} \\ B \implies \begin{cases} P = \sqrt{\dfrac{G_{cI}E_{11}t^3b^2}{12a^2}} \\ u = P\dfrac{8a^3}{bE_{11}t^3} \end{cases} \end{cases} \tag{D.1}$$

$$ENF\begin{cases} A \implies u = P\dfrac{3a_0^3+2l^3}{8bt^3E_{11}} \\ B \implies \begin{cases} P = \sqrt{\dfrac{G_{cII}16b^2t^3E_{11}}{9a^2}} \\ u = P\dfrac{3a^3+2l^3}{8bt^3E_{11}} \end{cases} \\ C \implies u = \dfrac{P}{96E_{11}I}\left[2l^3 - \dfrac{(64G_{cII}bE_{11}I)^{1.5}}{\sqrt{3}P^3}\right] \end{cases} \tag{D.2}$$

$$MMB\begin{cases} A \implies u = P\dfrac{4(3c-l)^2(a_0+\chi t)^3 + (c+l)^2\Big[3(a_0+0.42\xi t)^3+2l^3\Big]}{96l^2E_{11}I} \\ B \implies \begin{cases} P = \sqrt{\dfrac{G_{cM}64bl^2E_{11}I}{4(3c-l)^2(a+\chi t)^2+3(c+l)^2(a+0.42\chi t)^2}} \\ u = P\dfrac{4(3c-l)^2(a_0+\chi t)^3 + (c+l)^2\Big[3(a_0+0.42\chi t)^3+2l^3\Big]}{96l^2E_{11}I} \end{cases} \end{cases} \tag{D.3}$$

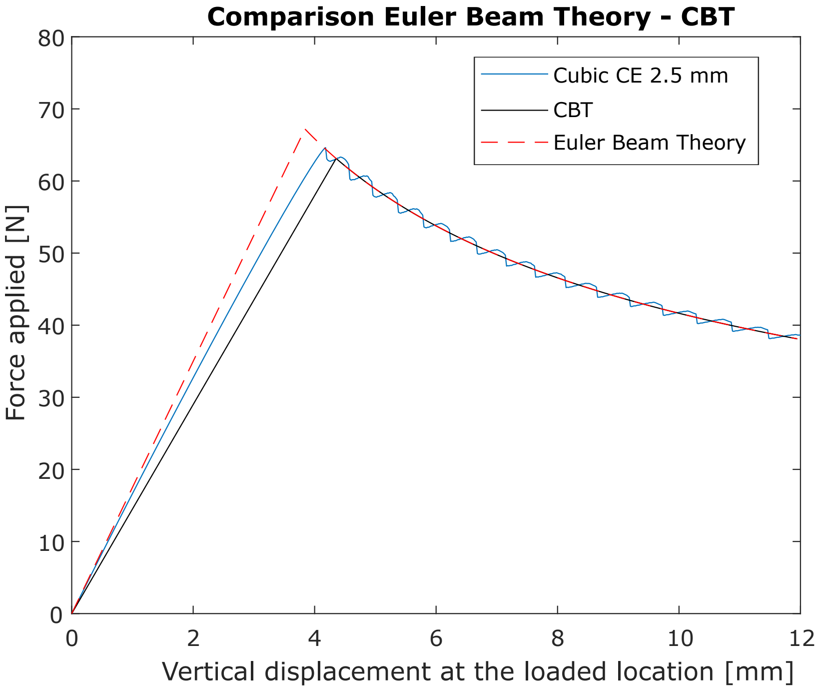

Figure D.2: Difference between EBT and CBT in the DCB test.

Where a_0 is the initial crack length, a is the propagated crack length, χ is a parameter evaluated with Equation D.4, t is the speciment thickness, E_{11} is the Young modulus in the longitudinal direction, I is the second moment of inertia of the substrate, G_c is the fracture toughness, b is the specimen width, l is the length of the specimen, c is the length of the lever used to assess a certain percentage of mixity of the opening in the MMB test.

$$\chi = \sqrt{\frac{E_{11}}{11G_{13}}\left[3 - 2\left(\frac{\Gamma}{\Gamma + 1}\right)^2\right]} \tag{D.4}$$

$$\Gamma = 1.18\frac{\sqrt{E_{11}E_{22}}}{G_{13}} \tag{D.5}$$

Where G_{13} is the shear modulus in the direction 1-3 and E_{22} is the Young modulus in the orthonal direction.

In Figure D.2 the difference between the Euler Beam Theory and the Corrected Beam Theory is depicted, together with the results coming from the 2.5 mm High Order CE mesh size.